Reply to Reviewer #1 (Maarten Krol)

This paper further develops and tests the inverse system introduced in part I of the paper. It contains interesting information, of which the POpULar system is particularly interesting. Unfortunately, the ability to provide complex correlation structures is not tested in the manuscript. Moreover, the study uses only artificial observations to test the system, which is OK for the current paper.

We really appreciate the reviewer, Prof. Dr. Maarten Krol, for taking his time to review our paper and giving us many valuable comments and suggestions. Described below are our replies to the reviewer's comments with page and line numbers of the attached supplementary manuscript, in which the changes from the original manuscript are colored in blue and red.

I have a few major/minor remarks, which need to be addressed before the paper can move on the GMD.

First, I have problems with the conclusion that the "non-exact" adjoint outperforms the linear model that uses the exact adjoint to calculate the derivative of the cost function. I think the result may be driven by the fact that the pseudo-observations have been produced by the model version with the flux-limiter activated. Thus it comes as no surprise that the non-exact flux-limited version of the model finds the solution more easy (the authors use a fixed number of iterations of 60). The problem with a non-exact adjoint appear when you want to estimate error-reductions, for which you to the best of my knowledge need an exact derivative (to approximate the Hessian). Anyhow, it would be interesting to include the views of the authors on the quantification of the error reduction and posterior co-variance calculation. As a note, I am not claiming that the non-exact adjoint produces erroneous results, but I am afraid the authors want to propagate the use of non-exact adjoint, which comes with disadvantages also. It would be instructive to repeat some experiments with pseudo-observations calculated with the flux-limiter turned off.

As the reviewer expected, the pseudo-observations are produced by the model with the flux limiter. Nevertheless, the model with the flux limiter may improve the model accuracy and, in fact, we found the better performance in the comparison with real observations as shown in the previous accompanying paper (Niwa et al. 2017). However, such improvement seems small. Furthermore, as the reviewer mentioned, the accuracy reduction induced by turning the flux limiter off could be compensated by smaller model time steps. Therefore, we have shifted the focus from the superiority of NONLINEAR to the comparable optimization performance, i.e., similar convergence speed, of NONLINEAR and LINEAR. Relevant modified/added sentences are as follows:

“It is found that a system of forward and adjoint models that has smaller model errors, but with nonlinearity has comparable optimization performance to that of another system that conserves linearity with an exact adjoint relationship.”
[Page 1, Lines 7-10]

“In fact, the flux limiter could improve the model accuracy due to its non-oscillatory property, but such improvement seems small in a CO2 transport simulation (Niwa et al., 2017). Also, the error induced by switching off the flux limiter could be compensated by smaller time steps, though it increases the computational cost.”
[Page 6, Lines 10-13]

“The forward simulation to construct the pseudo observations is performed with the online NICAM-TM with the flux limiter of the advection scheme turned on.”
[Page 8, Lines 23-24]

“This is due to the smaller transport error of the continuous adjoint and the flexibility of the POpULar optimization method against the model nonlinearity. Even with LINEAR, POpULar shows high optimization capability, though its error is slightly larger than when used with NONLINEAR.”
[Page 17, Lines 11-14]

Furthermore, as the reviewer suggested, we have repeated the experiment with pseudo-observations calculated with the flux limiter turned off. The inserted discussion is as follows.
“This is because the observations are constructed by the model with the flux limiter, which is more compatible with the NONLINEAR model set; that is, NONLINEAR has smaller model errors than LINEAR. In fact, when the observations are constructed

without the flux limiter, the GRMSE value from the LINEAR case becomes smaller and compa- rable to that of NONLINEAR (not shown). In this case, the GRMSE value from NONLINEAR does not change so much from the control case, suggesting that NONLINEAR is relatively insensitive to its model error in the optimization."
[Page 14, Lines 1-5]

We have also added some prospects about the posterior error estimate in Conclusions as
"For instance, the perfect adjoint relationship is desirable to approximate as accurately as possible the inverse Hessian that is defined as a symmetric matrix. In fact, an accurately approximated inverse Hessian can be considered as the posterior error covariance and can be applied to estimate error reductions and quantify observational impacts. A study into the application of the inverse Hessian matrix is in progress and will be reported elsewhere."
[Page 17, Lines 17-20].

The language needs refinement, preferably by a native speaker. Now, at many places, the optimal wording is not used to correctly phrase what the authors (in my opinion) want to say. I made many suggestions in the attached pdf. Especially sections 2.2.1 and 2.2.3 need to be clarified, since the strategy with respect to the biomass burning emissions remains unclear to me. Why is GFED left out of the true fluxes?
According to the reviewer's suggestions, we have modified the manuscript; especially, Sections 2.2.1 and 2.2.2 (previously 2.2.3) are thoroughly rewritten. Furthermore, we had a native speaker check again.

In fact, both the prior and true fluxes have biomass burning emissions but from different information sources: the prior biomass burning emission is from VISIT (as the part of NBP) and the true one is from GFED. These two biomass burning data are distinctly different because GFED is based on satellite fire spot data but VISIT uses only prognostic model-derived variables such as fuel load and soil moisture.
[Page 10, Lines 6-11]

What also should be clarified is the fact to the error setting of B is such that you assign larger errors at places where the flux sets differ. This leads to (artificial) good performance, because the system will adjust fluxes where differences are present, and will not adjust sources where no differences between the flux sets are present. I guess your statement: “Nevertheless, not including the biomass burning(s) in xtrue would help us to elucidate the ability of the inversion system to find large CO2 flux anomalies” gives a clue, but the description is simply messy, and needs improvement. To be more convincing, it would be good to repeat the inversion with a "proportional to emission" error, as commonly done in inversions, or using the "French" approach to set the error based on the emissions in neighbouring grid cells.

Why we used the prior-true flux differences for the prior error is that we wanted to simply validate the optimization scheme as a first step and also to evaluate the adjoint effects. Because the adjoint effects might depend on the setting of the prior error, the “true” prior error could provide a sort of benchmark result. As the reviewer pointed out, this leads an overestimation of the inversion performance. We touched on that in the first manuscript [Page 11, Lines 6-10], but we have added more in the revised manuscript to draw readers’ attention [Page 1, lines 6-7; Page 4, lines 13-15; Page 10, Lines 23-27; Page 11, lines 23-25; Page 18, lines 2-3].

Nevertheless, we also wanted to see the case when the prior flux errors are wrongly assigned. To this end, we did not use GFED to assign the flux errors. This results in that the general pattern of the prior flux error is “true”, but partially not “true”, where GFED’s emission is dominant.

Relevant descriptions we modified/added are as follows:

“Partially, we add errors into the prior flux errors by not including the biomass burning emission of GFED in Δx so that we can also see how the system works with wrongly defined prior errors. Therefore, Δx represents the flux differences between VISIT NBP and the modified CASA NEP for land, and between Iida et al. (2015) and Takahashi et al. (2009) for ocean.”

[Page 10, lines 27-30]

“Moreover, a remarkable performance of the new system is demonstrated by the result that the inversion is able to detect regionally limited flux anomalies caused by biomass burnings that are not represented in the prescribed prior errors.”

[Page 18, lines 4-5]

As the reviewer suggested, the “proportional to emission” error could be another way, but this strongly depends on which flux dataset we choose. In fact, we have already tried a prior error whose distribution is proportional to respiration or GPP component of the prior flux. Then, we found that the inversion performance significantly depends on the flux dataset, which makes it difficult to evaluate the adjoint effects. Therefore, we leave how to design the prior error covariance (not only variances but also covariances) for a future study.

technical, use "souce inversion" of "estimating sourcecs and sinks".

We have modified the text to “source/sink inversions of atmospheric constituents” [Page 1, line 1]

this depends on the measurement set-up, which you have not explained in the abstract.

According to the reviewer’s comment, we have added “when 65 weekly flask sampling observations at ground-based stations are used” at the end of the sentence. [Page 1, lines 11-12]

first explain a bit better....how synthesis inversion works...what this matrix is, etc...

We have added the sentence as follows.

“The synthesis inversion method takes an approach based on the Green’s function matrix, in which sub-continental scale regions are prescribed and the total flux for each region is set as a parameter.” [Page 2, lines 17-19]

I think the argument is that you have to limit the degrees of freedom, something you accomplish by introducing error correlations among the grid-cells

According to the comment, we have added the sentence as follows.

“Furthermore, introducing the flux error correlations reduces the degree of freedom and this may provide positive influences, e.g. reduction of noises, in a flux estimation, especially when observational networks are sparse.” [Page 3, lines 20-22]

? why would that be? Difficult Eigenvalue problem?

We wanted to say that a prior error covariance matrix with a higher dimension would require a much larger computational cost in an eigenvalue decomposition. To be more specific, we modified as

“However, eigenvalue decomposition that was used in Chevallier et al. (2007) or Meirink et al. (2008) would become difficult when the specified prior error covariance is complicated or time-consuming when the spatiotemporal resolution of fluxes is increased.” [Page 3, lines 22-24]

this statement is not true: this has not been proven if you refer to only one study.

According to the comment, we modified the text to be more general as,

“Therefore, which adjoint is better may depend on the assimilation settings.” [Page 4, lines 9-10]

unclear if the flux-limiter is used here (see main comment)

We have added a sentence saying that the pseudo observations are constructed by the online NICAM-TM with the flux limiter.

“The forward simulation to construct the pseudo observations is performed with the online NICAM-TM with the flux limiter of the advection scheme turned on. [Page 8, lines 23-24]

Furthermore, to introduce the flux limiter beforehand, we have moved the sentences for the flux limiter (and also for the continuous and discrete adjoint modes) from Section 2.3 [Page 12, lines 14-18] to Section 2.1.2 [Page 6 lines 6-lin 10].

not entirely true....I mean you also use a background term in the cont function.

Accordingly, we modified as

“…the prior fluxes, which are expected to get closer to the true fluxes.” and deleted the following sentence “The validity of the….”. [Page 8, lines 21-22]

at this stage it is good to mention that you also perturb the observations...!

According to the reviewer’s suggestion, we have moved the whole paragraph in the previous Section 2.2.2 (Pseudo observations) to the second paragraph of Section 2.2.

[Page 8, lines 24-29; Page 10, lines 14-21]

This is tricky: in fact, these numerical artifacts could be avoided by smaller time steps etc.

According to the reviewer's comment, we have added the following sentences into the third paragraph of Section 2.1.2, which was previously located in 2.3.

"In fact, the flux limiter could improve the model accuracy due to its non-oscillatory property, but such improvement seems small in a CO2 transport simulation (Niwa et al., 2017). Also, the error induced by switching off the flux limiter could be compensated by smaller time steps, though it increases the computational cost." [Page 6, lines 10-13]

chi2 ??? overfitting?

We have added discussion about the chi-square test from Page 14, line 34 to Page 15, line 10.

well, this sounds not really convincing. See my main comment (which I wrote before reading and understanding this part.).

We have modified the text as

"These results suggest that, under the assumption that the prior fluxes are well known, our new inversion system is capable of reproducing continental flux patterns by using only the surface observations." [Page 16, lines 3-5]

non-optimized case: what about more iterations?

These values do not significantly change when more iterations are performed. We can see that this experiment reaches almost close to the convergence after 60 iterations in Figure 3, which is newly added to show the cost function.

what about regions with zero prior?

error scales with emissions???

e.g. AUstralia...

OR IF THE ERROR IS

"MISSING BB ...LOGICAL RESULT

We did not scale the errors with the prior emissions, but used the prior-true flux differences as described in the text. In a future inversion study with real observations, we will use some prior flux information to construct prior errors (e.g., proportional to a prior flux), including biomass burning.

Other trivial changes:
Because the words “off-line”, “on-line”, “non-linear” are changed to “offline”, “online”, “nonlinear”, respectively, in the previous accompanying paper (Niwa et al., 2017) through the publication process, we have changed the text of this manuscript as well.

Reply to Reviewer #2

This paper describes the application of the POpULar minimization scheme within the 4dVAR analysis of CO2 fluxes. The topic is worthy of publication as a number of modelling issues are raised, however the use of an identical twin experiment with synthetic observations has its limitations. While such an approach is appropriate for testing a system, care needs to be taken regarding the strength of the conclusions. There are a number of corrections and clarifications that should be dealt with prior to final acceptance. Some revision is warranted prior to final acceptance.

We really appreciate the reviewer for taking her/his time to review our paper and giving us many valuable comments and suggestions. Described below are our replies to the reviewer's comments with page and line numbers of the attached supplementary manuscript, in which the changes from the original manuscript are colored in blue and red.

Specific issues:

1. A number of choices were made in the construction of the identical twin experiment that could unfairly favour one of the configurations over the other systems tested. These choices include:

- Using the same initial concentrations in the true and experimental run
- Having the true and prior land fluxes represent emissions with the same sources. The effect of these choices on the conclusions should be assessed.

Differently from NWP, the initial condition (concentrations) does not strongly affect observed spatiotemporal variations of CO2 concentrations, but the boundary condition (surface fluxes) dominantly affect those. This is because it has much longer assimilation window, i.e., 1-year-long, while NWP usually has a several-hours- to 1-day-long assimilation window. Therefore, we think the same initial concentrations in the true and experimental run is reasonable. Nevertheless, in an actual case, initial concentrations may have some errors. To cope with it, we will disregard optimized fluxes in early part of an assimilation window that have "absorbed" the errors of the initial concentrations. A corresponding description as below has been added in the revised manuscript.

“Optimizing only the surface fluxes is reasonable since these fluxes are the main driver of the atmospheric CO2 concentration variability. In “real” inversion analyses, there are errors in initial concentrations, but we can reduce their impact by disregarding the optimized fluxes during the early part of an assimilation window.”
[Page 9, lines 4-6]

Although the true and prior fluxes have the same sources (fossil fuel emission, terrestrial biosphere, air-sea exchange, and biomass burning emission), the data themselves have very different spatiotemporal patterns as shown in Figs. 7-10 (previously 6-9). Such deviations of the prior flux from the true flux are also likely in an actual case due to lack of our knowledge about CO2 fluxes. As Reviewer #1 suggested, we have thoroughly modified the flux descriptions of Section 2.2.1. Furthermore, we have added a description in Page 10 lines 3-6 (“General spatiotemporal variations … show distinct differences”) that corresponds to the above statement.

In summary, these experimental settings chosen in this study will not be serious concerns in an actual inversion analysis.

2. Initial concentrations are held fixed, and only fluxes are adjusted. This choice needs to be justified, especially if this system is to be cycled in an assimilation-forecast mode.
As described above, the initial concentrations do not affect CO2 concentration variations so much, which justifies the same initial concentrations. Furthermore, at this stage, we aim only at a surface flux inversion, not at an assimilation-forecast mode like NWP.

3. The background error variances are derived using the same truth as the experiment, Eq. 24, but in general the variances would also contain error, and probably significant errors since the method as described has no method of updating these.
We think that the prior (background) error variances we set in this experiment are too optimistic. However, we wanted to simply validate the optimization scheme as a first step and also to clarify the adjoint effects, which might depend on the setting of the prior error. We think the “true” prior error could provide a sort of benchmark result. We touched on the weakness of the prior error in the first manuscript [Page 11, Lines 6-10], but we have added more in the revised manuscript to draw readers’ attention [Page 1, lines 6-7; Page

4, lines 13-15; Page 10, Lines 23-27; Page 11, lines 23-25; Page 18, lines 2-3]. As stated earlier, we do not consider an assimilation-forecast cycle, therefore, there is no need so far for a method of updating the errors.

4. To better understand Fig 3 (Global RMSEplots vs. iteration) there should also be lines showing, cost function and its gradient. This is important for a number of reasons:
- All iterative schemes are run for 60 iterations – the importance of this is not established. Is the iterative process for each configuration close to convergence.
- Each configuration will have a different cost function value, so it is important to see how the different configurations compare in terms of cost functions.
- It would also be useful to check the standard Jmin diagnostic, given that the covariances are reasonably well known (by construction in an identical twin experiment)

We appreciate the reviewer's suggestion and agree the benefits of showing the cost functions. Accordingly, we have added the figure that shows the cost function vs. iteration for each experiment (Fig. 3). The added figure shows that, after 60 iterations, the off-diagonal cases are sufficiently converged and the diagonal cases are close to convergence [Page 13, lines 9-11]. Furthermore, we have added the discussion about the Jmin diagnostic, which is also suggested by Reviewer #1 [Page 14, line 34 – Page 15, line 10].

Figures: When comparing fields, it is much more instructive to compare show differences rather than full fields. Increments/differences are shown in Figure 4, but in 5, 6 & 7 only the full fields are shown, so it is quite possible to miss some important differences.

According to the reviewer's suggestion, we have changed Figure 6 (previously, Figure 5) from the full fields to the difference fields for the prior and posterior fluxes. For Figure 7, we made a figure that shows the difference fields as below, but found that the full fields look better. It is because the differences between the prior and true fluxes have magnitudes comparable to those of the true flux, which may mislead readers. The same goes for Fig. 8.

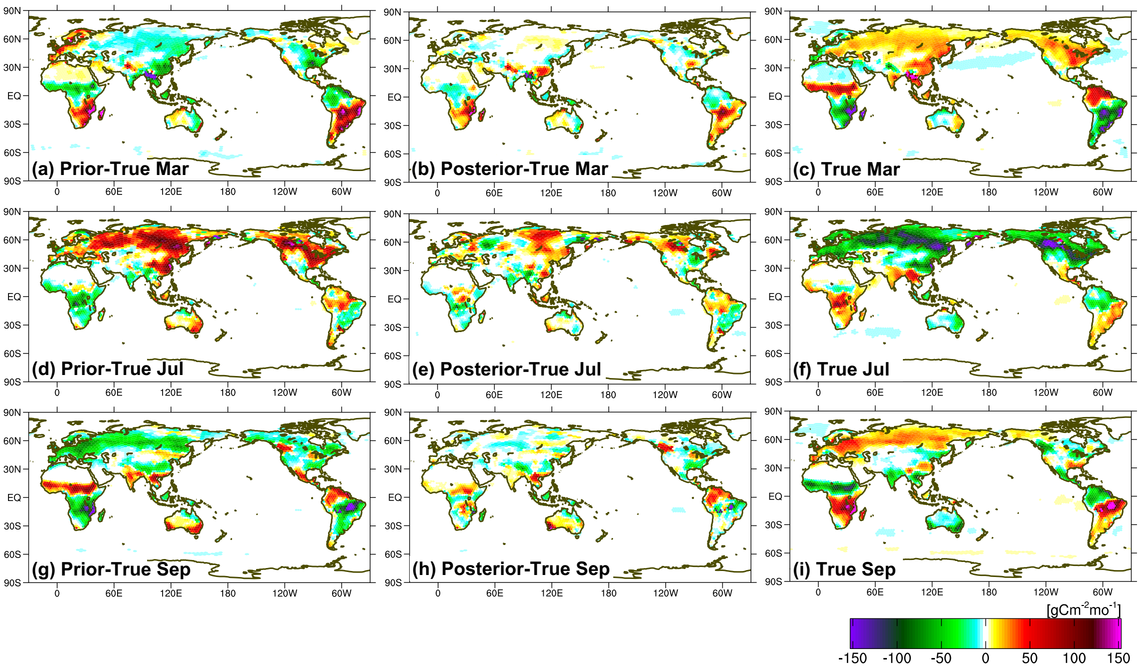

Figure: Same as Figure 6 of the previous manuscript, but showing differences between the prior/posterior and true fluxes.

Figures 8 & 9: Not sure why the lines need to be so thick. I would find it clearer if thinner lines were used – and easier to actually read values.

As suggested, we modified the figures with thinner lines.

Minor corrections:

Page 1, line 11: ". . .difficult decomposition of a matrix. . .". The standard decompositions used in variational assimilation are generally well-established not especially "difficult" in comparison with the development of other models described in this paper. The constraints on matrix structure imposed by the decompositions can be a problem – and so the key point is in the following sentence regarding the freedom to use a more general error covariance structure.

Unfortunately the paper uses a simple Gaussian correlation function, with one length scale for land and another for ocean, and no cross-correlation so the advantage is not investigated

- My underlying concern is that having the freedom to more generally specify error covariances is still some way from constructing a more general matrix and showing that it adds value – both in terms of accuracy and computational cost. There are a number of further potential problems that are not explored, and these may interact with the comparisons of the two adjoints explored in this paper

We have deleted “difficult”. [Page 1, line 14]

We agree that we have just introduced the optimization scheme and its advantage has not been explored. However, exploring the advantage of the optimization scheme is not a trivial task because, as the reviewer mentioned, a complicated error design may need a huge computational cost. The study for designing the flux error covariance is still in progress; therefore, we leave it for another paper. Corresponding descriptions are added in Page 11, lines 23-25, and Page 17, lines 27-30.

Page 2, line 17: While 4D-Var was implemented in operational NWP earlier than most other geophysical models, the theoretical basis goes back further, and so to say the 4D-Var was originally developed for NWP is incorrect. There were also 4D-Var ocean systems developed at a similar time.

We appreciate the reviewer’s thoughtful comments. Accordingly, we have modified the text as follows:

“The 4D-Var method has been employed in numerical weather prediction (NWP), in which a weather model’s initial state of the atmosphere is optimized, using observations, to improve weather prediction in many leading operational centers (e.g. Dee et al., 2011; Kobayashi et al., 2015). In NWP, the 4D-Var method is performed over successive time windows. The 4D-Var method has also been used in oceanography for a long time (e.g. Smedstad and O’Brien, 1991; Stammer et al., 2002; Usui et al., 2015).” [Page 2, lines 23-28]

Page2, line 22: “..and need to be resolved” is redundant

As suggested, we deleted it. [Page 2, line 32]

Page 3, line 2 & 3: It should be pointed out that nearly all global NWP systems also employ some level of ensemble covariances. These are considered important to:

- Capture some variation in time and space of background error variances and correlation
- Provide analysis error estimates.

Also while the error covariances are diagonal, these are in transformed variable space, which allows for some non-linear balances. The error covariance matrix of untransformed (physical) variables has off-diagonal elements. These latter variables are more akin to the fluxes being examined here.

We now understand that this discussion was shallow. For simplicity, we have deleted this discussion, not pointing out the details of the NWP situation. [Page 3, lines 14-15]

Page 3, line 5: There are problems with using a spectral decomposition for surface fluxes, but not allowing variables to be mutually correlated when they are close by is not one of them. Indeed the error correlation used here can be handled spectrally. The points that follow are valid, however the construction of useful, general correlations can add computational cost that is not explored here – and the effect of non-linear vs linear calculations could potentially be different.

We appreciate the reviewer's valuable comment. The discussion about the error correlation is elaborated as follows.

"In fact, Chevallier et al. (2012) found that the biosphere model they used to construct the prior CO2 flux has positive error correlations within certain spatiotemporal ranges, suggesting that the error correlations introduced in the prior error covariance matrix could propagate observational information to estimated flux values more effectively. Furthermore, introducing the flux error correlations reduces the degree of freedom and this may provide positive influences, e.g. reduction of noises, in a flux estimation, especially when observational networks are sparse."

[Page 3, lines 15-22]

As already stated, we agree that the construction of useful, general correlations may add an extra computational cost. We think sophisticating the design of the prior error covariance is not a trivial task and we leave it for a future study. This statement is added as

"As described above, we use idealized variances and simply define covariances to construct the prior error covariance matrix. In fact, the configuration of the prior error covariance significantly affects the performance of the inversion and a careful evaluation needs to be conducted, which we leave for a future study." [Page 11, lines 23-25]

Also, the computational discussion is also inserted in Conclusion of the revised manuscript as follows.
“However, it will not be a trivial task to appropriately design the prior error covariance in terms of accuracy and computational cost. A complicated flux error structure may require a considerable computational resource, even though POpULar requires only the matrix-vector multiplication with the prior error matrix. A further research effort in this direction is required.” [Page 17, lines 27-30]

Page 3, line 27: Guo and Sandu found that the results varied between tests using idealized data and real data. This should be a flag that care must be taken with interpreting results from the identical twin experiments conducted here.
We have detailed the result of Gou and Sandu (2011) a little bit more as

“However, when real observations were used in assimilation, they found that both the adjoint models showed similar performance, but the discrete adjoint performed slightly better than the continuous adjoint.”. [Page 4, lines 7-9]

Furthermore, a discussion of our result against their result is also added in Conclusion as
“The similar optimization performance of the continuous and discrete adjoint models achieved in this study is consistent with the assimilation result obtained by Gou and Sandu (2011) with real ozone observations.”. [Page 17, lines 14-15]

Page 3, line 31. It is not obvious to me where there was significant investigation into how the observation network could be better exploited – apart from the suggestion that the current network can provide sub-continental scale information, which seems a rather obvious comment to me.
Accordingly, we have modified the text as,
“…we also investigate how the current observation network could optimally constrain surface flux estimates.” [Page 4, lines 16-17]

Page 4, line 11: “. . .x represents the increment. . .”
Accordingly, we have corrected. [Page 4, line 28]

Page 11, line 19: typo: quadratic

We have corrected. [Page 13, 29]

Page 13, line 2: “Upon closer inspection. . .” would be better

As recommended, we have changed. [Page 15, line 27]

Other trivial changes:

Because the words “off-line”, “on-line”, “non-linear” are changed to “offline”, “online”, “nonlinear”, respectively, in the previous accompanying paper (Niwa et al., 2017) through the publication process, we have changed the text of this manuscript as well.

A 4D-Var inversion system based on the icosahedral grid model (NICAM-TM 4D-Var v1.0): 2. Optimization scheme and identical twin experiment of atmospheric CO_2 inversion

Yosuke Niwa[1], Yosuke Fujii[1], Yousuke Sawa[1], Yosuke Iida[2], Akihiko Ito[3], Masaki Satoh[4,5], Ryoichi Imasu[4], Kazuhiro Tsuboi[1], Hidekazu Matsueda[1], and Nobuko Saigusa[3]

[1]Oceanography and Geochemistry Research Department, Meteorological Research Institute, Tsukuba, Japan
[2]Global Environment and Marine Department, Japan Meteorological Agency, Tokyo, Japan
[3]Center for Global Environmental Research, National Institute for Environmental Studies, Tsukuba, Japan
[4]Atmosphere and Ocean Research Institute, The University of Tokyo, Kashiwa, Japan
[5]Japan Agency for Marine-Earth Science and Technology, Yokohama, Japan

Correspondence to: Y. Niwa (yniwa@mri-jma.go.jp)

Abstract. A 4-dimensional variational method (4D-Var) is a popular technique for ~~inverse modeling~~ source/sink inversions of atmospheric constituents, but it is not without problems. Using an icosahedral grid transport model and the 4D-Var method, a new atmospheric greenhouse gas (GHG) inversion system has been developed. The system combines ~~off-line~~ offline forward and adjoint models with a quasi-Newton optimization scheme. The new approach is then used to conduct identical twin experiments to investigate optimal system settings for an atmospheric CO_2 inversion problem, and to demonstrate the validity of the new inversion system. In this paper, the inversion problem is simplified by assuming the prior flux errors to be reasonably well known and by designing the prior error correlations with a simple function as a first step. It is found that a system of forward and adjoint models that has ~~less model errorsbut with non-linearity performs better than~~ smaller model errors, but with nonlinearity has comparable optimization performance to that of another system that conserves linearity with an exact adjoint relationship. Furthermore, the effectiveness of the prior error correlations is ~~confirmed;~~ demonstrated, as the global error is reduced by about 15 % by adding prior error correlations that are simply designed when 65 weekly flask sampling observations at ground-based stations are used. With the optimal setting, the new inversion system successfully reproduces the spatiotemporal variations of the surface fluxes, from regional (such as biomass burning) to ~~a global scale~~global scales. The optimization algorithm introduced in the new system does not require ~~difficult~~ decomposition of a matrix that establishes the correlation among the prior flux errors. This enables us to design the prior error covariance matrix more freely.

1 Introduction

Using the Bayesian algorithm, an inverse model estimates spatiotemporal variations of surface fluxes from ~~the~~ observations of atmospheric concentrations with the help of a priori information. ~~A~~ The power of such ~~technique has~~ techniques have been demonstrated in previous studies, such as the synthesis inversion analysis by Peylin et al. (2013) that demonstrated significant variations in regional carbon budgets at seasonal to interannual time scales.

In this study, we have developed a new inversion system based on the 4-dimensional variational (4D-Var) method. The 4D-Var method is a popular inversion method and has been widely used in inversion studies for atmospheric carbon dioxide (CO_2) (e.g. Chevallier et al., 2005; Rödenbeck, 2005; Baker et al., 2006a), methane (CH_4) (e.g. Bergamaschi et al., 2013) and carbon monoxide (CO) (e.g. Kopacz et al., 2010; Hooghiemstra et al., 2012).

Our primary interests are in long-lived greenhouse gases (GHGs) such as CO_2 and CH_4. Owing to strong ~~requirement~~ requirements for high-precision measurements necessary to identify changes in surface fluxes, observations of such atmospheric constituents ~~had~~ have been quite limited. ~~In the beginning, flask air sampling was adopted~~ At the start of CO_2 measurement programs, flask sampling was conducted mostly at background surface sites, with a typical ~~weekly sampling frequency~~ sampling frequency of one week (e.g. Conway et al., 1994). These data have been used in a synthesis inversion method (Enting, 2002) to estimate sub-continental scale CO_2 fluxes (e.g. Rayner et al., 1999; Gurney et al., 2002; Baker et al., 2006b). In recent decades, the global observation network of atmospheric GHGs has significantly expanded to include various measurement platforms. For example, *in situ* continuous observation measurements are now regularly taken at background stations, as well as at tall towers to infer regional continental fluxes (e.g. Sasakawa et al., 2010; Andrews et al., 2014). Moreover, worldwide aircraft observation programs ~~are now regularly conducted~~ have started to collect observations on a regular basis (e.g. Machida et al., 2008; Sawa et al., 2015; Matsueda et al., 2015), along with satellite observations dedicated to measurements of GHGs (Yoshida et al., 2013; Saitoh et al., 2016). These numerous GHG observational data can be exploited to estimate surface fluxes on a much finer scale than a sub-continental scale. ~~While the~~ The synthesis inversion method takes an approach based on the Green's function matrix, in which sub-continental scale regions are prescribed and the total flux for each region is set as a parameter. Therefore, the synthesis inversion method has limitations in resolution ~~, both in~~ both of fluxes and observations~~owing to its direct matrix calculation approach~~. In contrast, the 4D-Var method has nearly no limitation in the number of observations it can accommodate. The method also has the ability to estimate ~~model grid resolution fluxes~~fluxes at the resolution of the model grid, so that ~~regionally limited~~ regional CO_2 flux anomalies such as biomass burnings ~~are~~ become detectable. The 4D-Var method ~~was developed originally for~~ has been employed in numerical weather prediction (NWP), in which a weather model's initial state of the atmosphere is optimized, ~~with respect to a set of~~ using observations, to improve weather prediction ~~. This is done~~ in many leading operational centers (e.g. Dee et al., 2011; Kobayashi et al., 2015). In NWP, the 4D-Var method is performed over successive time windows. ~~At present, the~~ The 4D-Var method ~~is employed in many leading operational NWP centers~~has also been used in oceanography for a long time (e.g. Smedstad and O'Brien, 1991; Stammer et al., 2002; Usui et al., 2015). However, ~~because of~~ application of the 4D-Var method to GHGs inversion raises different issues than those associated with NWP since a much longer assimilation window ~~and the requirement of optimizing~~ is needed and we mainly optimize boundary conditions (surface fluxes), ~~but not~~ not necessarily the model's initial conditions (concentration fields)~~, application of the 4D-Var method to GHGs inversion raises different issues from those associated with NWP and need to be resolved~~.

In developing our 4D-Var inversion system, we have introduced unique numerical techniques that have not been used in previous 4D-Var inversions of GHGs; these techniques use an icosahedral grid transport model based on Non-hydrostatic Icosahedral Atmospheric Model (NICAM: Tomita and Satoh, 2004; Satoh et al., 2008, 2014), along with an efficient optimization scheme of Preconditioned Optimizing Utility for Large-dimensional analyses (POpULar: Fujii and Kamachi, 2003; Fujii, 2005). NICAM is one of the most advanced general circulation models (GCMs), with its dynamical frame structured with quasi-homogenous grids that are made by recursively dividing an icosahedron, which is completely different from the regular latitude-longitude grid models used so far. For the new inversion system, we have employed the NICAM-based Transport Model (NICAM-TM), naming our inversion system as NICAM-TM 4D-Var. The previous accompanying paper of ~~Niwa et al. (2016)~~ Niwa et al. (2017) derived and evaluated the ~~off-line~~ offline forward and adjoint models of NICAM-TM. This paper describes the entire NICAM-TM 4D-Var system, including the optimization scheme POpULar.

One prominent feature of POpULar is that it does not require ~~inverse calculation of the~~ the inversion of a large prior error covariance ~~. Generally, an~~ matrix. Although the Bayesian inversion algorithm generally requires the inverse matrix of a prior error covariance~~is included in the Bayesian inversion algorithm. However~~, its direct calculation is infeasible due to its large matrix size. Therefore, previous studies have avoided the inverse matrix calculation by simply neglecting the off-diagonal elements of the prior error covariance or employing eigenvalue decomposition (Chevallier et al., 2007; Meirink et al., 2008). Actually, the off-diagonal elements represent the error ~~correlation~~ correlations among prior fluxes in space and time. ~~In NWP, the spectral method is often used and the prior error covariance is defined in the spectral field, thus able to regard the prior error covariance as diagonal. However, it cannot be applied to the flux inversion problem. Although designing flux error correlations is not a trivial task, it needs to be addressed because surface fluxes must be mutually correlated when they are located in a close proximity to each other (Chevallier et al., 2012). Additionally, it is possible~~ In fact, Chevallier et al. (2012) found that the biosphere model they used to construct the prior CO_2 flux has positive error correlations within certain spatiotemporal ranges, suggesting that the error correlations ~~could more effectively~~ introduced in the prior error covariance matrix could propagate observational information to estimated flux values ~~.~~ more effectively. Furthermore, introducing the flux error correlations reduces the degree of freedom and this may provide positive influences, e.g. reduction of noises, in a flux estimation, especially when observational networks are sparse. However, eigenvalue decomposition that was used in Chevallier et al. (2007) or Meirink et al. (2008) would become difficult when the specified prior error covariance is complicated or time-consuming when the spatiotemporal resolution of fluxes is increased. Since the POpULar optimization scheme does not require eigenvalue decomposition, we can easily introduce flux error correlations into the inverse calculation. POpULar was developed originally for oceanography assimilation (Usui et al., 2006, 2015); our study is its first application to an ~~inverse problem of atmospheric trace constituent~~atmospheric trace gas inverse problem.

In order to validate and verify the new inversion system, we have conducted identical twin experiments of atmospheric CO_2 inversion, in which pseudo, instead of real, observations produced by “true fluxes” are assimilated~~, instead of real observations~~. It has been demonstrated that such an identical twin experiment is an effective way to test the ability of an optimization scheme in an inversion calculation (e.g. Baker et al., 2006a; Chevallier et al., 2007; Yumimoto and Takemura, 2013; Liu et al., 2014). ~~Conducting~~ By conducting sensitivity tests based on the identical experiment, we investigate ~~the~~ optimal system settings in the context of adjoint models and optimization schemes. In addition, we demonstrate the utility of introducing error correlations in the prior fluxes.

As described in ~~Niwa et al. (2016)~~Niwa et al. (2017), NICAM-TM has two types of adjoint models: one is a discrete adjoint model and the other is a continuous one. The discrete adjoint model ensures model linearity and maintains an exact adjoint relationship with its corresponding forward model, while the continuous adjoint model is ~~non-linear~~ nonlinear and consequently loses the exact adjoint relationship but has less model errors. Gou and Sandu (2011) compared a continuous adjoint model with a corresponding discrete adjoint model using a regional chemical transport model and evaluated the effect of using these two models in the optimization of initial states of tropospheric ozone. In that study, they found the continuous adjoint to be superior in ideal assimilation cases~~, especially when observations are sparse~~. However, when real observations were used in assimilation, they found that ~~the~~ both the adjoint models showed similar performance, but the discrete adjoint performed slightly better than the continuous adjoint. Therefore, which adjoint is better ~~depends strongly on models used. Furthermore, it may also~~ may depend on the assimilation settings. Approaching the problem differently from Gou and Sandu (2011) when applied to CO_2, we try to optimize surface fluxes of CO_2, which has a much longer lifetime in the atmosphere and hence requires a longer assimilation window than ozone. In this study, we evaluate the effect of using discrete and continuous adjoint models as applied to CO_2 inversion problems. ~~Using the~~ Practically, the inversion performance depends on various conditions. Therefore, as a first step, we assume the prior flux errors to be well known. This ideal assumption certainly overvalues the performance of the system, but it would clarify the effect of the adjoint models. Furthermore, using the optimal inversion settings determined from the sensitivity tests with the ideal prior flux errors, we also investigate how the current observation network could ~~be exploited better to~~ optimally constrain surface flux estimates.

2 Methods

2.1 NICAM-TM 4D-Var

2.1.1 System overview

An inversion problem employs Bayes' theorem, and an optimal solution of control variable **x** is obtained where the cost function defined below is minimized.

$$J(\mathbf{x}) = \frac{1}{2}\mathbf{x}^{\mathrm{T}}\mathbf{B}^{-1}\mathbf{x} + \frac{1}{2}\left(\mathbf{M}\mathbf{x} - \mathbf{y}^{\mathrm{dobs}}\right)^{\mathrm{T}}\mathbf{R}^{-1}\left(\mathbf{M}\mathbf{x} - \mathbf{y}^{\mathrm{dobs}}\right), \qquad (1)$$

where **B** is the prior error covariance matrix of **x**, **M** is the forward transport model operator matrix which links surface fluxes to atmospheric concentration measurements taken at specified locations and time, and **R** is the error covariance matrix of the misfit between observations and modeled concentrations. It should be noted here that **M** is assumed linear according to the linear property of atmospheric transport, though we use both linear and ~~non-linear~~ nonlinear models as described in Section 2.3 below. The control variable vector **x** represents the increment from the prior flux $\mathbf{x}^{\mathrm{pri}}$ and the observation vector $\mathbf{y}^{\mathrm{dobs}}$ represents differences between the modeled concentrations from $\mathbf{x}^{\mathrm{pri}}$ and observed concentrations $\mathbf{y}^{\mathrm{obs}}$, i.e., $\mathbf{y}^{\mathrm{dobs}} = \mathbf{y}^{\mathrm{obs}} - \mathbf{M}\mathbf{x}^{\mathrm{pri}}$. In fact, the control variable vector **x** consists of initial concentrations as well as surface fluxes, thus atmospheric concentration fields are uniquely determined in the model. However, for simplicity, we only optimize surface fluxes in this study. In the 4D-Var method, the optimal **x** is determined after iterative calculations that uses the gradient of the cost function with respect to **x**

$$\mathbf{g} = \mathbf{B}^{-1}\mathbf{x} + \mathbf{M}^{\mathrm{T}}\mathbf{R}^{-1}\left(\mathbf{Mx} - \mathbf{y}^{\mathrm{dobs}}\right). \tag{2}$$

The last term on the right-hand side is derived by a forward simulation **Mx** followed by an adjoint simulation $\mathbf{M}^{\mathrm{T}}\mathbf{R}^{-1}\left(\mathbf{Mx} - \mathbf{y}^{\mathrm{dobs}}\right)$, which are performed by the forward and adjoint models of NICAM-TM, respectively. Both the forward and adjoint models are driven by archived meteorological data (e.g. mass fluxes, temperatures, turbulent coefficients, cumulus base mass fluxes; details are found in ~~Niwa et al. (2016)~~Niwa et al. (2017)). The meteorological data are prepared by a GCM run of NICAM, in which horizontal winds are nudged towards reanalysis data to simulate real atmospheric flow fields.

In summary, Fig. 1 shows a schematic figure of the NICAM-TM 4D-Var system. In practice, the 4D-Var calculations are conducted as follows:

(i) Run the on-line NICAM with nudging to make meteorological data that are used in the following simulations of the forward and adjoint NICAM-TM,

(ii) Run the forward NICAM-TM to calculate atmospheric concentration fields of a target atmospheric constituent forced by prior flux data,

(iii) Calculate the differences between the modeled and observed concentrations,

(iv) Run the adjoint NICAM-TM to calculate the gradient of the cost function from the model-observation differences that are weighted by the error covariance of observation-model misfit, and

(v) Modify the prior flux data according to the cost function and its gradient using the POpULar optimization scheme.

The prior flux data are replaced with those given by (v), and then the (ii)-(v) calculation steps are repeated until the flux data are sufficiently optimized according to a convergence criterion. Finally, the optimized flux is ~~treated~~ called as the posterior flux.

2.1.2 NICAM-TM

NICAM achieves consistency between tracer transport and air density change, which assures Lagrangian conservation and mass conservation simultaneously, owing to its finite volume method-based dynamical frame (Satoh et al., 2008; Niwa et al., 2011a). This property is absolutely necessary for transport simulations of long-lived tracers such as GHGs. Because of this, NICAM-TM has been developed and used for transport and inversion studies of CO_2 (Law et al., 2008; Patra et al., 2008; Niwa et al., 2011b, 2012; Peylin et al., 2013). Its fundamental transport performances have been evaluated satisfactorily using observations of radon (^{222}Rn) and sulfur hexafluoride (SF_6) (Niwa et al., 2011a, 2012).

Detailed descriptions of the ~~off-line~~ offline forward and adjoint models of NICAM-TM are found in the accompanying paper of ~~Niwa et al. (2016)~~Niwa et al. (2017). Reanalysis data used with nudging in the ~~on-line~~ online calculation are from the 6-hourly Japan Meteorological Agency Climate Data Assimilation System (JCDAS) reanalysis (Onogi et al., 2007). The archived meteorological data consist of air mass densities, three-dimensional air mass fluxes, vertical diffusion coefficients, mixing ratios of water substances, temperatures, and cumulus base mass fluxes. These data are consistent with the dynamical calculation of NICAM, though their temporal resolutions are decreased from the original model time step (20 min.) to 1- to 3-hourly steps in the ~~off-line model calculations (Niwa et al., 2016)~~offline model calculations (Niwa et al., 2017). The horizontal resolution is set as "glevel-5" (5 denotes the number of division from the original icosahedron; see Fig. 1 of ~~Niwa et al. (2016)~~Niwa et al. (2017)), whose grid interval is about 240 km, and the number of vertical model layers is 40.

As described in Niwa et al. (2017), NICAM-TM has the option of running either in the discrete or continuous adjoint mode. The linearity of the discrete adjoint is ensured and the perfect adjoint relationship is achieved with the forward model in which the nonlinear flux limiter (Thuburn, 1996) in the advection calculation is turned off. In contrast, the continuous adjoint has the same nonlinear flux limiter as that of the forward model calculation to maintain the monotonicity of the advection adjoint, but this fails to achieve the perfect adjoint relationship with the forward model. In fact, the flux limiter could improve the model accuracy due to its non-oscillatory property, but such improvement seems small in a CO_2 transport simulation (Niwa et al., 2017). Also, the error induced by switching off the flux limiter could be compensated by smaller time steps, though it increases the computational cost. Using the identical twin experiment described later, we conduct sensitivity tests to elucidate some of the impacts on the inversion results due to the differences in the adjoint models (discrete or continuous), details of which are described in Section 2.3.

2.1.3 POpULar

For optimization, we use the scheme of POpULar (Fujii and Kamachi, 2003; Fujii, 2005). The POpULar scheme is based on the optimizing scheme developed by Derber and Rosati (1989) (hereafter DR89). Fujii and Kamachi (2003) extended the linear conjugate gradient method of DR89 to ~~non-linear~~ nonlinear cases using a quasi-Newton method.

In Eqs. (1) and (2), the matrix size of $\mathbf{B}$ is too large to be inverted if $\mathbf{B}$ is an off-diagonal matrix, i.e., when prior error correlations are considered. Therefore, a transformation of the control variables is often applied, with one prominent transformation being $\tilde{\mathbf{x}} = \mathbf{B}^{-1/2}\mathbf{x}$. This transformation provides efficient preconditioning to accelerate the convergence of iterative calculations (Lorenc, 1988). In fact, several 4D-Var inversion systems for atmospheric trace gas constituents employ this transformation with eigenvalue decomposition (Chevallier et al., 2007; Meirink et al., 2008), though feasibility of eigenvalue decomposition still depends on the matrix size and the designing of the error correlations. In contrast, DR89 and POpULar also use the preconditioning of Lorenc (1988) but they do not require eigenvalue decomposition. ~~Detailed~~ The detailed algorithm of DR89 is described in Appendix A. Below we describe the POpULar scheme but readers are encouraged to ~~see~~ consult Fujii (2005) for further explanation.

The quasi-Newton scheme of POpULar employs the limited-memory version (Nocedal, 1980; Liu and Nocedal, 1989) of the Broyden-Fletcher-Goldfarb-Shanno formula (L-BFGS) that updates the search direction $\mathbf{d}$ of the control variable $\mathbf{x}$ using an approximated inverse Hessian of $J(\equiv \mathbf{H})$. Using the transformation of Lorenc (1988) ($\tilde{\mathbf{x}} = \mathbf{B}^{-1/2}\mathbf{x}$), the transformed control variable is updated in iterative calculations as

$$\tilde{\mathbf{x}}_k = \tilde{\mathbf{x}}_{k-1} + \alpha_k \tilde{\mathbf{d}}_{k-1}, \tag{3}$$

$$\tilde{\mathbf{d}}_k = -\tilde{\mathbf{H}}_{k,0}\tilde{\mathbf{g}}_k, \tag{4}$$

where k is the iteration counter, $\tilde{\mathbf{d}} = \mathbf{B}^{-1/2}\mathbf{d}$, $\tilde{\mathbf{g}} = \mathbf{B}^{1/2}\mathbf{g}$, and $\tilde{\mathbf{H}}_{k,0} = \mathbf{B}^{-1/2}\mathbf{H}_{k,0}\mathbf{B}^{-1/2}$. The coefficient α_k is the step length of the line search that minimizes $J(\mathbf{x}_{k-1} + \alpha_k \mathbf{d}_{k-1})$. If an optimization problem is highly ~~non-linear~~nonlinear, α_k is iteratively sought with quadratic interpolation (Fujii, 2005). However, in a linear or weakly ~~non-linear~~ nonlinear problem, such as the one considered here in this study, the initial guess of $\alpha_k = 1$ is valid at most iterations. ~~By~~ Using the L-BFGS formula, $\tilde{\mathbf{H}}_{k,0}$ is calculated with m pairs of $\tilde{\mathbf{y}}_k (= \tilde{\mathbf{g}}_k - \tilde{\mathbf{g}}_{k-1})$ and $\tilde{\mathbf{p}}_k (= \tilde{\mathbf{x}}_k - \tilde{\mathbf{x}}_{k-1})$ that are derived from the previous iterations as

$$\tilde{\mathbf{H}}_{k,-m} = \gamma_k \mathbf{I}, \tag{5}$$

$$\tilde{\mathbf{H}}_{k,l} = \tilde{\mathbf{V}}^{\mathrm{T}}_{k+l}\tilde{\mathbf{H}}_{k,l-1}\tilde{\mathbf{V}}_{k+l} + \tilde{\rho}_{k+l}\tilde{\mathbf{p}}_{k+l}\tilde{\mathbf{p}}^{\mathrm{T}}_{k+l}, \qquad (l = -m+1, \cdots, -1, 0), \tag{6}$$

where $\mathbf{I}$ is the identity matrix, $\tilde{\rho}_k = 1/\tilde{\mathbf{y}}^{\mathrm{T}}_k\tilde{\mathbf{p}}_k$ and $\tilde{\mathbf{V}}_k = \mathbf{I} - \tilde{\rho}_k\tilde{\mathbf{p}}_k\tilde{\mathbf{y}}^{\mathrm{T}}_k$. γ_k represents the scaling coefficient (Shanno and Phua, 1978) calculated as

$$\gamma_k = \tilde{\mathbf{y}}^{\mathrm{T}}_k\tilde{\mathbf{p}}_k / \tilde{\mathbf{y}}^{\mathrm{T}}_k\tilde{\mathbf{y}}_k. \tag{7}$$

Using non-transformed variables, the above Eqs. (5)-(7) are simply rewritten by replacing $\mathbf{I}$ with $\mathbf{B}$ as

$$\mathbf{H}_{k,-m} = \gamma_k \mathbf{B}, \tag{8}$$

$$\mathbf{H}_{k,l} = \mathbf{V}^{\mathrm{T}}_{k+l}\mathbf{H}_{k,l-1}\mathbf{V}_{k+l} + \rho_{k+l}\mathbf{p}_{k+l}\mathbf{p}^{\mathrm{T}}_{k+l}, \qquad (l = -m+1, \cdots, -1, 0), \tag{9}$$

where $\rho_k = 1/\mathbf{y}^{\mathrm{T}}_k\mathbf{p}_k$ and $\mathbf{V}_k = \mathbf{I} - \rho_k\mathbf{p}_k\mathbf{y}^{\mathrm{T}}_k$, and

$$\gamma_k = \mathbf{y}^{\mathrm{T}}_k\mathbf{p}_k / \mathbf{y}^{\mathrm{T}}_k\mathbf{z}_k, \tag{10}$$

where $\mathbf{z}_k = \mathbf{B}\mathbf{y}_k = \mathbf{h}_k - \mathbf{h}_{k-1}$ and $\mathbf{h}_k = \mathbf{B}\mathbf{g}_k$. Then, the search direction can be expressed as a linear combination of $\mathbf{h}$, $\mathbf{z}$, and $\mathbf{p}$ as

$$\mathbf{d}_k = -\gamma_k\mathbf{h}_k + \sum_{l=-m+1}^{0}\left(a_{k,l}\mathbf{z}_{k+l} + b_{k,l}\mathbf{p}_{k+l}\right), \tag{11}$$

where $a_{k,l}$ and $b_{k,l}$ are the scalar coefficients that are determined by $\mathbf{h}_k$ and m pairs of $\mathbf{p}$ and $\mathbf{z}$ (details are described in Appendix B). It should be noted here that Eq. (11) does not require ~~$\mathbf{B}^{-1}$ calculation~~ the calculation of $\mathbf{B}^{-1}$. In order to avoid the calculation of $\mathbf{B}^{-1}$, we introduce $\mathbf{c}_k = \mathbf{B}^{-1}\mathbf{x}_k$, $\mathbf{q}_k = \mathbf{B}^{-1}\mathbf{p}_k$, and $K_k = \frac{1}{2}\mathbf{x}_k\mathbf{B}^{-1}\mathbf{x}_k$. The cost function and its gradient at iteration k are written as

$$J(\mathbf{x}_k) = K_k + \frac{1}{2}\left(\mathbf{M}\mathbf{x}_k - \mathbf{y}^{\mathrm{dobs}}\right)^{\mathrm{T}}\mathbf{R}^{-1}\left(\mathbf{M}\mathbf{x}_k - \mathbf{y}^{\mathrm{dobs}}\right), \tag{12}$$

$$\mathbf{g}_k = \mathbf{c}_k + \mathbf{M}^{\mathrm{T}}\mathbf{R}^{-1}\left(\mathbf{M}\mathbf{x}_k - \mathbf{y}^{\mathrm{dobs}}\right). \tag{13}$$

Along with the updating of $\mathbf{x}$ by

$$\mathbf{x}_k = \mathbf{x}_{k-1} + \alpha_k \mathbf{d}_k = \mathbf{x}_{k-1} + \mathbf{p}_k, \tag{14}$$

K_k can ~~be also~~ also be recursively updated as

$$K_k = K_{k-1} + \mathbf{p}_{k-1}^{\mathrm{T}} \left(\mathbf{c}_{k-1} + \frac{1}{2}\mathbf{q}_{k-1} \right). \tag{15}$$

Furthermore, $\mathbf{c}_k$ and $\mathbf{q}_k$ can be updated using Eqs. (14) and (11) respectively as

$$\mathbf{c}_k = \mathbf{c}_{k-1} + \mathbf{q}_{k-1}, \tag{16}$$

$$\mathbf{q}_k = \alpha_k \mathbf{B}^{-1} \mathbf{d}_k = \alpha_k \left(-\gamma_k \mathbf{g}_k + \sum_{l=-m+1}^{0} \left(a_{k,l} \mathbf{y}_{k+l} + b_{k,l} \mathbf{q}_{k+l} \right) \right). \tag{17}$$

In practice, POpULar uses the above equations of (10)–(17) with the initial condition of

$$\mathbf{x}_0 = \mathbf{0}, \tag{18}$$

$$K_0 = 0, \tag{19}$$

$$\mathbf{c}_0 = \mathbf{0}, \tag{20}$$

$$\mathbf{g}_0 = \mathbf{M}^{\mathrm{T}} \mathbf{R}^{-1} \left(\mathbf{M}\mathbf{x}_0 - \mathbf{y}^{\mathrm{dobs}} \right), \tag{21}$$

$$\mathbf{h}_0 = \mathbf{B}\mathbf{g}_0, \tag{22}$$

$$\mathbf{d}_0 = -\mathbf{h}_0. \tag{23}$$

Thus, we can see that the sequence of these equations do not require $\mathbf{B}^{-1}$. Practical calculations of Eqs. (11) and (17) are described in Appendix B.

2.2 Identical twin experiment design

The identical twin experiment is designed for an atmospheric $\mathrm{CO_2}$ inversion. We first run a forward simulation to construct a set of pseudo atmospheric observations using a prescribed flux dataset considered as “true fluxes”. In the experiment, a different flux dataset is used as the prior fluxes and the pseudo observations are assimilated into the system to modify the prior fluxes, which ~~is expected to converge~~ are expected to get closer to the true fluxes. ~~The validity of the inversion system can be elucidated by evaluating how close the posterior fluxes have approached the true fluxes after the assimilation.~~

The forward simulation to construct the pseudo observations is performed with the online NICAM-TM with the flux limiter of the advection scheme turned on. After a three-year spin-up, concentration values are extracted at 65 locations that emulate well-known $\mathrm{CO_2}$ ground-based observation sites (locations are shown in Fig. 2 and the corresponding detailed information is listed in Appendix C). Although some sites actually operate *in situ* continuous observations, we assume weekly sampling at all the sites for simplicity. Therefore, the total number of observation data is 65 (sites) $\times$ 52 (weeks) = 3,380. To sample well-mixed air masses, the timing of flask sampling is set at 13:00 LST at each site. Random values with a standard deviation of 0.2 ppm are added to the extracted model values to mimic actual measurement uncertainties.

The analysis period, i.e., the assimilation window, is chosen as the year ~~of~~ 2010 and monthly mean CO$_2$ fluxes are optimized in the inversion. Therefore, the number of control variables to be optimized is 12 (months) × 10,242 (the number of horizontal grid points) = 122,904. Since we do not optimize the initial concentrations, we use the same initial concentrations for the true and assimilation runs. Optimizing only the surface fluxes is reasonable since these fluxes are the main driver of the atmospheric CO$_2$ concentration variability. In "real" inversion analyses, there are errors in initial concentrations, but we can reduce their impact by disregarding the optimized fluxes during the early part of an assimilation window.

2.2.1 True and prior flux datasets

~~We have prepared a prior flux dataset that will be used in future inversions with real atmospheric observations. But for this study, we have prepared the true flux dataset mentioned above, terrestrial fluxes of which are already optimized to some extent by another inversion and explicitly includes biomass burning data.~~ Table 1 summarizes the prior and true flux datasets. All of the prior and true flux data are provided as monthly ~~mean. As commonly done for~~ means. Both for the prior and true fluxes, we use the same fossil fuel emissions of Carbon Dioxide Information Analysis Center (CDIAC) (Andres et al., 2013) ~~. Thus,~~ and we assume that the fossil fuel emissions in the prior flux dataset is perfectly known~~and~~ . Therefore, fluxes other than the fossil-fuel emissions are optimized in the ~~inversion~~identical twin experiment.

~~For terrestrial biosphere and ocean fluxes, the prior flux dataset uses net biome production (NBP) data from a process-based ecosystem model called Vegetation Integrative SImulator for Trace Gases (VISIT: Ito and Inatomi, 2012), and sea-air exchange data based on shipboard ΔpCO$_2$ measurements calculated by Japan Meteorological Agency (Iida et al., 2015), respectively.~~

For the true flux dataset, we use the net ecosystem production (NEP) data of the Carnegie-Ames-Stanford-Approach (CASA) model (Randerson et al., 1997) modified by the inversion of Niwa et al. (2012)~~and~~ , and the climatological ΔpCO$_2$-based sea-air exchange data of ~~Takahashi et al. (2009). The true flux dataset also contains biomass burning emissions from the Global Fire Emissions Database (GFED) version 3.1 (van der Werf et al., 2010). The reason of~~ Takahashi et al. (2009). The reason for the inversion modification of the CASA flux field is that the original CASA NEP is annually balanced (that is, annually integrated flux is zero everywhere). Therefore, ~~we scaled~~ to be more realistic, we scale the terrestrial flux values at each latitude band and month ~~so~~ such that the zonal average value coincides with ~~a more realistic value~~ that of the inversion flux~~calculated by Niwa et al. (2012).~~ The true flux dataset also contains biomass burning emissions from the Global Fire Emissions Database (GFED) version 3.1 (van der Werf et al., 2010). ~~The inversion flux is the average for 2006–2008, in which the global terrestrial biosphere uptake is 4.4 Pg C yr^{-1}. Readers should note that NEP of CASA and NBP of VISIT represent different fluxes; in addition to NEP, NBP has additional sources of biospheric respiration and combustion emissions caused by natural and anthropogenic disturbances. By replacing the original CASA fluxes with the inversion fluxes and adding the biomass burning emissions, both the true and prior land fluxes represent emissions with same sources.~~

For the prior terrestrial fluxes, we use net biome production (NBP: NEP + disturbance emissions such as biomass burnings) data from a process-based ecosystem model called Vegetation Integrative SImulator for Trace Gases (VISIT: Ito and Inatomi, 2012). For the prior ocean fluxes, we use sea-air exchange data based on shipboard ΔpCO$_2$ measurements calculated by Japan

Meteorological Agency (Iida et al., 2015), which is slightly modified by replacing the undefined fluxes in marginal seas with the fluxes from Takahashi et al. (2009).

General spatiotemporal variations of the integrated true and prior fluxes described above can be compared with the posterior fluxes shown in Figs. 7-10. Both the true and prior ocean fluxes are based on the shipboard ΔpCO_2 measurements, and thus have similar spatial patterns. However, there are significant differences in their seasonal patterns, as shown in Fig. 9. While the true and prior terrestrial fluxes have much larger magnitudes than the ocean fluxes, they do show distinct differences. Those differences are attributable not only to the different biosphere models used but also to the biomass burnings (GFED and the part of VISIT NBP). To evaluate biomass burning emission, GFED utilizes satellite fire spot data, while VISIT uses only prognostic model-derived variables such as fuel load and soil moisture (Kato et al., 2013). Although VISIT cannot sufficiently represent the actual spatial patterns of biomass burning due to the stochasticity of wildfire regime, regional emission amounts are comparable to those of GFED.

For the global terrestrial and ocean areas, the annual net uptakes of the true flux are 2.4 and 1.4 Pg C, respectively. Meanwhile, those of the prior flux are 3.3 and 2.3 Pg C, respectively.

2.2.2 ~~Pseudo observations~~

~~Pseudo observations are constructed from the on-line calculation using NICAM-TM driven by the true flux dataset. After a three-year spin-up, concentration values are extracted at 65 locations that emulate well-known CO_2 ground-based observation sites (locations are shown in Fig. 2 and detail information is listed in Appendix C). Although some sites actually operate *in situ* continuous observations, we assume, for simplicity, that flask air sampling observations are made at all the sites with one-week sampling frequency. Therefore, the total number of observation data is 65 (sites) × 52 (weeks) = 3,380. The timing of flask sampling is set at 13:00 LST at each site for sampling in well-mixed air masses. Random values with a standard deviation of 0.2 ppm are added to the extracted model values to mimic actual measurement uncertainties.~~

2.2.2 Prior error covariance

~~Diagonal~~ In this study, we simplify the inversion problem by using idealized prior errors. Specifically, the diagonal elements of **B** (variance) are ~~derived from absolute~~ set proportional to the differences between the prior and true fluxes ~~that are~~ ($\Delta\mathbf{x}$), with the assumption that the prior flux errors are well known. However, in reality, this is too optimistic because we do not know the true flux errors in an actual inversion analysis. However, this simplification enables us to easily verify the validity of the optimization scheme introduced in this study and highlight the effects of the adjoint models in the sensitivity tests. Partially, we add errors into the prior flux errors by not including the biomass burning emission of GFED in $\Delta\mathbf{x}$ so that we can also see how the system works with wrongly defined prior errors. Therefore, $\Delta\mathbf{x}$ represents the flux differences between VISIT NBP and the modified CASA NEP for land, and between Iida et al. (2015) and Takahashi et al. (2009) for ocean. To construct the diagonal elements of **B**, the $\Delta\mathbf{x}$ is scaled for specified global land and ocean total values as

$$B_{i,i} = \left(r \underline{|} |\Delta x\underline{^{\mathrm{pri}}_{i} - x^{\mathrm{true}}_{i}|} |_{i} \right)^{2}, \tag{24}$$

where i ~~denote~~ denotes the element index, and r is the scaling factor. ~~x^{pri} and x^{true} represent the prior and true flux values, respectively, but at this stage we exclude the biomass burnings of GFED from the true fluxes.~~ The scaling factor r is determined so that the annual global uncertainty

$$\sigma = \sqrt{\mathbf{aBa}^{\mathrm{T}}} \tag{25}$$

corresponds to 3.0 Pg C yr^{-1} and 0.5 Pg C yr^{-1} for land and ocean fluxes, respectively. The vector **a** acts as the spatiotemporal averaging operator and **ax** produces the annual global average of **x**. ~~In fact, using the difference between $\mathbf{x}^{\mathrm{pri}}$ and $\mathbf{x}^{\mathrm{true}}$ provides some ideal error variance distributions, although $\mathbf{x}^{\mathrm{true}}$ does not include the biomass burnings of GFED. When using real observations, $\mathbf{x}^{\mathrm{true}}$ is of course unknown. Therefore, this ideal error covariance would overestimate the performance of the inversion system. We recognize that the prior variance setting critically influences the optimization quality; however, the task of seeking appropriate variances is out of the scope of this study. Nevertheless, not including the biomass burnings in $\mathbf{x}^{\mathrm{true}}$ would help us to elucidate the ability of the inversion system to find large CO$_2$ flux anomalies.~~

For the off-diagonal elements in matrix **B** (covariance), we introduce a simple spatial correlation with the Gaussian function ~~in the off-diagonal elements (covariance)~~ as

$$B_{i,j} = B_{i,i}B_{j,j}\exp\left(-\frac{l_{i,j}^2}{2L^2}\right), \quad i \neq j, \tag{26}$$

where $l_{i,j}$ is the horizontal length between i and j and L is the correlation scale length. Here, we assume no temporal correlation since we are optimizing relatively low temporal resolution fluxes (monthly means). In Eq. (26), we use the globally unique scale lengths for land and ocean, L_{lnd} and L_{ocn}, set at 500 km and 1000 km, respectively. There is no cross correlation between land and ocean fluxes. These correlation scale lengths are determined from the results of previous studies (such as Rödenbeck, 2005; Chevallier et al., 2007; Basu et al., 2013), although they did not use the Gaussian function as in Eq. (26) but used instead an exponential decay function. ~~As is the case with the variance, we leave the determination of optimal values for L for a future study.~~ Figure 2 shows four examples of the error correlation distributions determined by $\exp(-l^2/2L^2)$ with $L_{\mathrm{lnd}} = 500$ km and $L_{\mathrm{ocn}} = 1000$ km.

As described above, we use idealized variances and simply define covariances to construct the prior error covariance matrix. In fact, the configuration of the prior error covariance significantly affects the performance of the inversion and a careful evaluation needs to be conducted, which we leave for a future study.

2.2.3 Observation-model misfit error covariance

We set the error covariance for model-observation misfit **R** at 1 ppm^2 (ppm is used here as equivalent to the dry air mole fraction unit of μmol mol^{-1}) for all the variances and 0 ppm^2 for all the covariances; therefore, **R** is a unit diagonal matrix. Actually, introducing off-diagonal elements in **R** is difficult compared to **B** because the inverse calculation of **R** is necessary at some stage in the calculation. Nevertheless, the "no covariance" assumption is relatively reasonable considering the sparse spatiotemporal distribution of the observations used here. The misfit uncertainty of 1 ppm is arbitrary but reasonable in representing model-observation misfits, based on the reported numbers published in previous studies (e.g. Patra et al., 2008).

2.2.4 Diagnostic measures

After the assimilation, we evaluate how close the posterior fluxes approach the true fluxes, by using root-mean-square error (RMSE) measures described below. On the global scale, we use

$$\mathrm{GRMSE} = \sqrt{\frac{1}{N}\frac{1}{12}\sum_{i=1}^{N}\sum_{m=1}^{12}\left(x_{i,m}^{\mathrm{post}} - x_{i,m}^{\mathrm{true}}\right)^2}, \tag{27}$$

where i and m denote the i^{th} model grid and the m^{th} month, respectively, and N denotes the number of model grids. x^{post} represents the posterior flux value and x^{true} denotes the true flux value~~ including the biomass burnings~~. We also investigate error distributions by

$$\mathrm{RMSE}_i = \sqrt{\frac{1}{12}\sum_{m=1}^{12}\left(x_{i,m}^{\mathrm{post}} - x_{i,m}^{\mathrm{true}}\right)^2}, \tag{28}$$

calculated for each model grid i.

2.3 Sensitivity tests

~~Using the above~~ Using the above-described identical twin experiment, we ~~conducted sensitivity tests to elucidate impacts on the inversion results due to the differences in the adjoint models (discrete or continuous) and optimization schemes.~~ conduct sensitivity tests around the adjoint model, the optimization scheme and the prior error covariance as follows.

~~As described in Niwa et al. (2016), the linearity of the discrete adjoint is ensured and the perfect adjoint relationship is achieved with the forward model in which the non-linear flux limiter (Thuburn, 1996) in the advection calculation is turned off. On the other hand, the continuous adjoint has the same non-linear flux limiter as that of the forward model calculation to maintain the monotonicity of the advection adjoint. Although this fails to achieve perfect adjoint relationship with the forward model, smaller model transport errors are obtained. Therefore, we have tested~~ We test two forward and adjoint model sets: one set preserves linearity and complete adjoint relations using the forward model ~~without~~ with the flux limiter turned off in the advection scheme and the discrete adjoint model (LINEAR), while the other one is a ~~non-linear~~ nonlinear and non-exact adjoint set using the forward model with the flux limiter on and the continuous adjoint model (~~NON-LINEAR~~NONLINEAR).

Originally, the POpULar optimization scheme was designed for ~~non-linear~~ nonlinear problems of ocean dynamics by modifying the linear optimization scheme of DR89, as described ~~above~~in Section 2.1.3. In atmospheric CO_2 inversions, the atmospheric transport process is treated as linear, i.e., tracer is passive, and ~~non-linear chemical process is~~ nonlinear chemical processes are not involved. ~~Meanwhile~~However, if we use the ~~NON-LINEAR~~ NONLINEAR model set, the problem becomes slightly ~~non-linear~~ nonlinear due to the use of the flux limiter. Therefore, we also examine the ~~behaviors~~ behavior of the linear (DR89) and ~~non-linear~~ nonlinear (POpULar) optimization schemes with the two model sets (LINEAR and ~~NON-LINEAR~~NONLINEAR).

Furthermore, we also compare results between the two ~~case, with~~ cases involving diagonal **B** and ~~with~~ off-diagonal **B**, to confirm the effectivity of prior error correlations. In the diagonal **B** case, we set the off-diagonal elements to zero and rescale the diagonal elements by r (Eq. 24) ~~so~~ such that the global uncertainty σ (Eq. 25) ~~coincides with~~ equals that of the off-diagonal **B**. In summary, we conduct eight sensitivity tests using the LINEAR/~~NON-LINEAR~~ NONLINEAR model sets, the DR89 and POpULar optimization schemes and diagonal and off-diagonal **B** (Table 2).

3 Results

3.1 Sensitivities to adjoint models, optimization schemes, and error correlations

In each of the sensitivity tests, we perform a total of 60 iterations to optimize the surface fluxes. Figure 3 shows ~~GMRSE~~ the cost function variations against the number of iterations~~and~~. Similarly, Fig. 4 shows the GRMSE variations against the number of iterations; Table 2 lists GRMSE values after 60 iterations. ~~As the iterative calculation proceeds, GRMSE shows smooth reduction~~ Figure 3 indicates that 60 iterations are sufficient to achieve convergence for the off-diagonal cases (Figs. 3c and d) and close to convergence for the diagonal cases (Figs. 3a and b), with the exception involving the NONLINEAR+DR89 case with the diagonal **B**. Similarly, GRMSE shows a smooth reduction as the iterative calculation proceeds in all the cases except for the case of ~~NON-LINEAR~~NONLINEAR+DR89 with the diagonal **B** (Fig. ~~3a~~4a), where the GRMSE reduction in value matches that of its corresponding LINEAR case. But after about 30 iterations, the two curves diverge rapidly as the ~~NON-LINEAR~~ NONLINEAR case increases in GRMSE to a value at the 60th iteration that is greater than the value at the beginning of the iteration. This is due to the fact that DR89 is strictly designed for a linear problem (Appendix A) and hence is incompatible with ~~NON-LINEAR~~NONLINEAR. However, if ~~off-diagonal~~ the covariances are included in **B**~~is used, NON-LINEAR~~, NONLINEAR+DR89 produces a GRMSE reduction curve similar to that of the LINEAR case (Fig. ~~3c~~4c). This may be due to the fact that the smoothing effect of the error correlation in **B** suppresses the incompatibility of DR89 with ~~NON-LINEAR~~the NONLINEAR model set.

~~On the other hand,~~ POpULar does not show such incompatibility with ~~NON-LINEAR~~ NONLINEAR (Figs. ~~3b~~ 4b and d). This is because the POpULar optimization algorithm allows model ~~non-linearity~~nonlinearity. For the LINEAR cases, the GRMSE values from the use of POpULar are the same as those in the DR89 cases, irrespective of the prior error covariance setting (Table 2).

~~Although the differences are modest, NON-LINEAR generates smaller GRMSE values than those from LINEAR while using POpULar, which is apparent especially with the off-diagonal **B** (Fig. 3d). This is because of the smaller model error property of the NON-LINEAR model set. In the non-linear~~ In all the cases except DR89 with the diagonal **B**, the LINEAR and NONLINEAR model sets show similar convergence speed, suggesting that there is almost no difference in the optimization ability between these two sets (Figs. 3b-e). In the nonlinear case, the cost function defined by Eq. (1) is no longer ~~quadractic~~ quadratic and the minimum point is not uniquely determined. Therefore, use of the ~~NON-LINEAR~~ NONLINEAR model set has a risk of falling into a local minimum, causing deterioration of the optimization~~. The result indicates that , for the CO$_2$ inversion problem considered here,~~ , but we find that it is not the case in our inversion experiment. We note that NONLINEAR generates smaller GRMSE values than those generated by LINEAR while using POpULar, the ~~smaller model error of NON-LINEAR surpasses the negative effect of its non-linearity.~~ differences, although modest, are noticeably with the off-diagonal **B** (Fig.

4d). This is because the observations are constructed by the model with the flux limiter, which is more compatible with the NONLINEAR model set; that is, NONLINEAR has smaller model errors than LINEAR. In fact, when the observations are constructed without the flux limiter, the GRMSE value from the LINEAR case becomes smaller and comparable to that of NONLINEAR (not shown). In this case, the GRMSE value from NONLINEAR does not change so much from the control case, suggesting that NONLINEAR is relatively insensitive to its model error in the optimization.

Comparing Figs. ~~3c~~ 4c and d with Figs. ~~3a~~ 4a and b, we see that the off-diagonal **B** produces significantly smaller GRMSE than the diagonal **B**. The reduction ratio in GRMSE from the prior value (5.59×10~~$^{-7}$~~$^{-7}$ mol m^{-2} s^{-1}) increases by about 15 %; the GRMSE value reduces from 4.07–4.10$\times10^{-7}$ mol m^{-2} s^{-1} (excluding the case of ~~NON-LINEAR~~NONLINEAR+DR89) to 3.21–3.37$\times10^{-7}$ mol m^{-2} s^{-1} by introducing the error correlation in **B**. An implication of this result, especially for the global ocean, is that the diagonal **B** fails to reduce GRMSE from the prior condition (Table 2). Intrinsically, the optimization of the ocean fluxes is difficult compared to that of the land fluxes, because ocean flux variations are much smaller than those associated with the land, but also in our case we use a true ocean flux that is similar to the prior flux. The result indicates that introducing spatial error correlations in **B** is necessary in order to modify such small ocean fluxes.

~~Figure 4~~ Figure 5 shows RMSE distributions of the posterior fluxes calculated with the diagonal and off-diagonal **B**; the RMSE distribution of the prior flux is also shown as a reference. Posterior fluxes are produced after 60 iterations using POpULar+~~NON-LINEAR~~NONLINEAR. As already indicated in Figs. ~~3c~~ 4c and d, the RMSEs of the two posterior fluxes are much ~~less~~ smaller than that of the prior, demonstrating the optimization skill of our new system. The prior flux has RMSE ~~much more than~~ exceeding 15$\times10^{-7}$ mol m^{-2} s^{-1} in the terrestrial areas, where biosphere activity is large (e.g., eastern North America, South America, East and Southeast Asia, and Africa) (Fig. ~~4d~~5d). Those errors are effectively reduced by the assimilation to values mostly less than 10$\times10^{-7}$ mol m^{-2} s^{-1}. Moreover, in the off-diagonal **B** case, the errors are further reduced, especially in the areas where observations are sparse, e.g., Africa, South Asia, South America, and Australia (Fig. ~~4c~~5c). This indicates that introducing error correlations allows an effective propagation of atmospheric CO_2 information to surface fluxes located beyond the observation footprints that are determined by atmospheric flow fields.

3.2 Posterior flux features

In this section, we present general features of the posterior fluxes and compare them with the true fluxes. We assess when, where and how much the posterior fluxes are reliable when real observations are used. The posterior fluxes analyzed here are derived after 60 iterations by ~~NON-LINEAR~~NONLINEAR+POpULar with the off-diagonal **B**, which has been shown to display the smallest error among the above eight sensitivity tests.

First, we compare atmospheric CO_2 concentration fields that are generated by the forward NICAM-TM from the true, prior and posterior fluxes. Figure ~~5a~~ 6a shows the time series of simulated atmospheric concentrations at the Minamitorishima (MNM) ~~observation~~ observational site, located on western North Pacific. In fact, the pseudo observation network (Appendix C) includes MNM and its location is shown in Fig. 2. In Fig. ~~5a~~6a, we see a good agreement between the posterior and the observational concentration values. The root mean square difference between them is 0.19 ppm, which is much less than the prescribed model-observation misfit error of 1 ppm (Section 2.2~~.4). This follows from the fact that we have~~ .3). To see more overall consistency of the inversion, χ^2 is calculated from the minimum of the cost function ($J_{\min}$) as

$$\chi^2 = \frac{2J_{\min}}{m}, \tag{29}$$

where m is the number of observations (=3380). Although the theoretically expected value of χ^2 is 1 (Tarantola, 2005), our experiment results in $\chi^2 = 0.08$ ($J_{\min} = 131$). This is because we have a perfect transport simulation ~~.~~ (i.e. the model error is zero). That is, the same transport model is used for preparing the observations and the assimilation. ~~The~~ Consequently, the prescribed value of 1 ppm ~~is rather inflated~~ for the observation-model misfit error is rather conservative (but reasonable for a practical inversion with real observations)~~, but it is expected that the difference between the posterior and observed concentration is close to the random error of~~. In fact, when we repeat the experiment with 0.2 ppm ~~that we add to the observations(Section 2.2.2).~~ observation-model misfit errors with which we perturb the observations, we obtain a value of $\chi^2 = 0.89$ ($J_{\min} = 1496$), much closer to 1.

~~Figures 5b-d~~ Figures 6b-d show latitude-time cross sections of zonally averaged surface concentration simulated from the true ~~, prior and posterior fluxes.~~ flux field (Fig. 6b), its differences from the concentration field generated by the prior flux (Fig. 6c), and by the posterior flux (Fig. 6d). Compared to the zonally averaged concentration field generated from the true fluxes, a period of low concentration at the northern latitudes starts one month earlier in the field forced by the prior fluxes. Furthermore, latitudinal gradients between 30°S and 30°N are weaker during January–May. These features are modified by the assimilation so that the spatiotemporal variation of the posterior CO_2 concentration is nearly identical to the ~~one~~ concentration variations obtained from the true flux field (Fig. ~~5d~~6d).

To see the degree of similarity in the flux distribution between the posterior and true fluxes, we show monthly mean flux distribution for March, July and September of 2010 in Fig. ~~6~~7, along with the corresponding prior fluxes. As shown in ~~Fig. 6~~the figure, the general pattern of the true flux for each month is retrieved relatively well, as indicated in the posterior flux distribution, from the prior flux.

For March, the true flux has larger sources in the northern mid- to high-latitudes than those of the prior flux and this feature is retrieved well by the inversion (Figs. ~~6a-c~~7a-c). Furthermore, it is noteworthy that the inversion successfully retrieves the distinct source/sink contrast patterns around the equator in Africa and South America. For July, the true flux shows a larger biosphere sink in the northern latitudes than the ~~one captured by the~~ prior flux; the posterior flux calculated by our inversion method shows a sink of similar magnitude as ~~detected in~~ the true flux (Figs. ~~6d-f~~7d-f). However, there ~~is~~ remains a mismatch in the spatial distribution of the sink. Upon closer ~~look~~inspection, one can see that the posterior flux has large sinks in West Siberia and eastern North America (Fig. ~~6e~~7e), while the true flux has a comparably large sink in western Canada (Fig. ~~6f~~7f). During the summer season, the vertical transport over a continental region is quite active, and the emission from the surface ~~becomes~~ is well mixed in the vertical. Therefore, this causes the ground-based stations to observe only diluted flux signals, resulting in weak ~~constraint~~ constraints on the flux estimation. For September, the prior flux is still characterized by sinks over most of the continental regions. However, the true flux has already changed to a source in the northern high-latitudes, and the posterior flux is able to reproduce that feature (Figs. ~~6g-i~~7g-i). Moreover, the distinct source/sink contrasts in Africa and South America, signs of which are opposite to those in March, are again well retrieved by the inversion. The ideal prior error variance (Section 2.2~~.3~~.2) might have helped this achievement to some extent. Using ~~differences~~ the difference between the true and prior fluxes to determine the prior error variance allows the system to know where and by how much observational signals should propagate to surface fluxes. ~~But it is not able to assign the sign of the flux (source or sink), only the magnitude. Therefore, these~~ These results suggest that, under the assumption that the prior fluxes are well known, our new inversion system is capable of reproducing continental flux patterns ~~from surface observationsonly~~by using only the surface observations.

~~Furthermore, the inversion is able to detect successfully~~ Furthermore, even when the prescribed prior flux errors are wrong, the inversion system is capable of obtaining reasonable flux estimates, given that “hot spot”-like CO_2 sources from biomass burnings have been successfully detected. In Fig. ~~7~~8, we focus on the fluxes in Indochina for March, and in South America and Africa for September of 2010. In those regions, the true fluxes derived from GFED show regional ~~anomalies~~distinct anomalies compared to VISIT, but they are not used to assign the prior error variance (Section 2.2.2). In 2010, large biomass burnings occurred under a severe dry condition in Amazon (Lewis et al., 2011). Compared to the prior fluxes that have moderate spatial variations, the posterior fluxes show large sources in those areas that are comparable to the true flux patterns, though the posterior source peaks are underestimated in Thailand and Amazon, and are shifted from the coast to the inland area in southern Africa. ~~It should be noted that in this exercise, we do not use biomass burning information to assign the prior error variance (Section 2.2.3). Therefore, these results suggest that our new inversion system is capable of detecting even regionally limited flux anomalies . Such capability~~ The capability to detect such flux anomalies will be enhanced if more observations are available.

~~Figure 8~~ Figure 9 compares zonally-integrated seasonal cycles of the posterior fluxes over terrestrial and ocean areas in three latitudinal bands with those of the prior and true fluxes. As expected from Fig. ~~6~~7, the seasonal cycle of the posterior flux agrees generally well with that of the true flux, compared to that of the prior flux. However, the degree of agreement is latitudinally dependent. The region where the amplitude and the phase of the seasonal cycle of the posterior flux agree the most with those of the true flux is in the northern mid- to high-latitude band (30–90°N) (Figs. ~~8a~~ 9a and b), for both the land and the ocean. The result reflects the ~~existence of~~ relatively dense surface ~~observation~~ observational network in this latitude zone. The seasonal cycles of the posterior fluxes in the other latitudinal bands (30°S–30°N and 30–90°S) show moderate similarities to the true flux seasonal cycles. The largest difference can be seen for the ocean flux in the 30–90°S latitude band, particularly during the southern hemisphere fall season. Improvements could be made, but the seasonal amplitudes are very small and are difficult to ~~be retrieved~~retrieve.

Latitudinal profiles of annual zonal mean fluxes can also be retrieved well (Fig. ~~9~~10). For example, compared to the prior flux, the posterior flux matches the true flux and shifts the sink towards lower latitudes (Fig. ~~9a~~10a). Moreover, the true and posterior fluxes consistently show two distinct source peaks across the equator. Figure ~~9b~~ 10b shows that this flux pattern is due mostly to the terrestrial flux (Fig. ~~9b~~10b). In the southern extra tropics, on the other hand, the posterior flux is not modified significantly from the prior flux, suggesting weak constraints due to a sparse number of observational stations in that area. Compared to the terrestrial flux, the ocean flux has much smaller latitudinal variations (Fig. ~~9c~~10c). In spite of such small variations, we see improvements in the prior flux by the inversion in the northern latitudinal band of 30–60°N and in the

Southern Ocean in the latitudinal band of 50–70°S. At other latitudes, the posterior flux has similar profiles to those of the prior flux.

4 Conclusions

In this paper, we have introduced, described and tested our new 4D-Var inversion system based on the icosahedral grid model, NICAM. Adding to the ~~off-line~~ offline forward and adjoint models of NICAM-TM, this study has introduced the optimization method of POpULar, which constitutes an essential part of the 4D-Var system. Moreover, we have conducted identical twin experiments to confirm the capability and utility of the new system for atmospheric CO_2 inversion.

Based on the results of the sensitivity tests using various combinations of the optimization method (DR89 and POpULar) and the discrete and continuous adjoint models (LINEAR and ~~NON-LINEAR~~NONLINEAR), we have found that a combination of POpULar and the continuous adjoint (~~NON-LINEAR~~NONLINEAR+POpULar) ~~has produced the least~~ leads to the smallest error. This is due to the ~~less~~ smaller transport error of the continuous adjoint and the flexibility of the POpULar optimization method against the model ~~non-linearity. Even with the discrete adjoint~~nonlinearity. Even with LINEAR, POpULar shows high optimization capability, ~~but~~ though its error is slightly larger than when used with ~~the continuous adjoint. Therefore, if~~ NONLINEAR. The similar optimization performance of the continuous and discrete adjoint models achieved in this study is consistent with the assimilation result obtained by Gou and Sandu (2011) with real ozone observations. If model linearity and perfect adjoint relationship are strongly required, the combination of LINEAR+POpULar could be ~~another choice.~~ a sensible choice. For instance, the perfect adjoint relationship is desirable to approximate as accurately as possible the inverse Hessian that is defined as a symmetric matrix. In fact, an accurately approximated inverse Hessian can be considered as the posterior error covariance and can be applied to estimate error reductions and quantify observational impacts. A study into the application of the inverse Hessian matrix is in progress and will be reported elsewhere.

We have introduced spatial error correlations with the simple Gaussian function in the off-diagonal elements of the prior error covariance and have shown that it significantly improves the posterior fluxes, reducing the global flux error by about 15 %. This result is consistent with other 4D-Var inversions, but we have achieved it an easier way that does not require matrix inverse calculation nor any matrix decomposition; the optimization algorithm of POpULar has an advantage in its simple treatment of the off-diagonal matrix. This would prove to be a more powerful tool when more complicated flux error structures are considered. For instance, Meirink et al. (2008) assumed that the spatial and temporal correlations are mutually independent, but POpULar would enable us to consider cross correlations in space and time. However, it will not be a trivial task to appropriately design the prior error covariance in terms of accuracy and computational cost. A complicated flux error structure may require a considerable computational resource, even though POpULar requires only the matrix-vector multiplication with the prior error matrix. A further research effort in this direction is required. In this study, arbitrary numbers and ~~an~~ ideal prior errors have been used respectively for the error correlation scales and the diagonal elements (variance) of the prior error covariance matrix. Therefore, our next stage of research will involve an investigation of optimal prior error design, taking the advantage of POpULar.

By using our new 4D-Var inverse system, we have successfully retrieved general features of the true flux variations from weekly flask observations obtained from 65 ground-based stations, though with the assumption that the prior flux errors are reasonably well known. Moreover, a remarkable performance of the new system is demonstrated by the result that the inversion is able to detect regionally limited flux anomalies caused by biomass burnings that are not represented in the prescribed prior errors. However, even with the perfect (non-biased) transport model and the ideal prior error variances, improvements in the prior flux estimate in some regions have been found to be limited due to the sparseness of the observations. Further improvements are expected by adding data from *in situ* continuous measurements and worldwide observations by aircraft (e.g. Machida et al., 2008) and satellites (e.g. Yoshida et al., 2013; Saitoh et al., 2016) in a future study.

Code availability

Development of NICAM-TM 4D-Var and experimental studies of its application are being continued by the authors. The source codes of NICAM-TM 4D-Var are available for those who are interested. The source codes of NICAM-TM are included in the package of the parent model NICAM, which can be obtained upon request under the general terms and conditions (http://nicam.jp/hiki/?Research+Collaborations). The source code of POpULar is also accessible by contacting Yosuke Fujii of Meteorological Research Institute (http://www.mri-jma.go.jp/Member/oc/kefujiiyosukefu_en.html).

Appendix A: Optimization scheme of Derber and Rosati (1989)

The conjugate gradient method with the preconditioning of $\tilde{\mathbf{x}} = \mathbf{B}^{-1/2}\mathbf{x}$ uses the following equations:

$$\tilde{\mathbf{x}}_k = \tilde{\mathbf{x}}_{k-1} + \alpha_k \tilde{\mathbf{d}}_{k-1}, \tag{A1}$$

$$\beta_k = \tilde{\mathbf{g}}_k^{\mathrm{T}} \tilde{\mathbf{y}}_k / \tilde{\mathbf{d}}_{k-1}^{\mathrm{T}} \tilde{\mathbf{y}}_k, \tag{A2}$$

$$\tilde{\mathbf{d}}_k = -\tilde{\mathbf{g}}_k + \beta_k \tilde{\mathbf{d}}_{k-1}. \tag{A3}$$

With the non-transformed variables, the above equations can be rewritten as

$$\mathbf{x}_k = \mathbf{x}_{k-1} + \alpha_k \mathbf{d}_{k-1}, \tag{A4}$$

$$\beta_k = \mathbf{h}_k^{\mathrm{T}} \mathbf{y}_k / \mathbf{d}_{k-1}^{\mathrm{T}} \mathbf{y}_k, \tag{A5}$$

$$\mathbf{d}_k = -\mathbf{h}_k + \beta_k \mathbf{d}_{k-1}. \tag{A6}$$

Here we should note that neither $\mathbf{B}^{-1}$ nor $\mathbf{B}^{1/2}$ is ~~not~~ required, but only the multiplication $\mathbf{h}_k = \mathbf{B}\mathbf{g}_k$ is calculated. If a linear problem is considered, Eq. (A5) is written as

$$\beta_k = \mathbf{h}_k^{\mathrm{T}} \mathbf{g}_k / \mathbf{h}_{k-1}^{\mathrm{T}} \mathbf{g}_{k-1}, \tag{A7}$$

and this is used in DR89. Introducing $\mathbf{e} = \mathbf{B}^{-1}\mathbf{d}$, the step length α_k is calculated as

$$\mathbf{f}_k = \mathbf{e}_{k-1} + \mathbf{M}^{\mathrm{T}}\mathbf{R}^{-1}\mathbf{M}\mathbf{d}_{k-1}, \tag{A8}$$

$$\alpha_k = -\mathbf{g}_{k-1}^{\mathrm{T}} \mathbf{d}_{k-1} / \mathbf{d}_{k-1}^{\mathrm{T}} \mathbf{f}_k. \tag{A9}$$

Differently from POpULar, Eq. (A9) gives the analytical solution of α_k. If the cost function J is convex quadratic, i.e., linear problem, α_k can be derived analytically by

$$\alpha_k = -\mathbf{g}_{k-1}^{\mathrm{T}}\mathbf{d}_{k-1}/\left(\mathbf{d}_{k-1}^{\mathrm{T}}\mathbf{Q}\mathbf{d}_{k-1}\right), \tag{A10}$$

where $\mathbf{Q}$ is the Hessian of J ($= \mathbf{B}^{-1} + \mathbf{M}^{\mathrm{T}}\mathbf{R}^{-1}\mathbf{M}$) (Nocedal and Wright, 2006). One may easily find the above equation is the same as Eq. (A9). Such an analytical calculation of α_k is the so-called exact line search. After the updates of $\mathbf{x}$ with Eq. (A4) and $\mathbf{d}$ with Eq. (A6), $\mathbf{g}$ and $\mathbf{e}$ are updated as

$$\mathbf{g}_k = \mathbf{g}_{k-1} + \alpha_k \mathbf{f}_k, \tag{A11}$$

$$\mathbf{e}_k = -\mathbf{g}_k + \beta_k \mathbf{e}_{k-1}. \tag{A12}$$

Starting from the initial condition of

$$\mathbf{x}_0 = \mathbf{0}, \tag{A13}$$

$$\mathbf{g}_0 = \mathbf{M}^{\mathrm{T}}\mathbf{R}^{-1}\mathbf{d}^{\mathrm{dobs}}, \tag{A14}$$

$$\mathbf{h}_0 = \mathbf{B}\mathbf{g}_0, \tag{A15}$$

$$\mathbf{d}_0 = -\mathbf{h}_0, \tag{A16}$$

$$\mathbf{e}_0 = -\mathbf{g}_0, \tag{A17}$$

equations (A4)–(A12) are repeatedly calculated until the values of $\mathbf{x}$ are converged enough to a pre-defined convergence criterion.

Appendix B: Practical calculations of d and q

Practical derivations of $\mathbf{d}_k$ and $\mathbf{q}_k$ (Eqs 11 and 17) are as follows:

$$\mathbf{s}_0 = -\mathbf{h}_k, \tag{B1}$$

$$\mathbf{t}_0 = -\mathbf{g}_k, \tag{B2}$$

$$\mathbf{s}_{l-1} = \mathbf{s}_l - \rho_{k+l}\mathbf{t}_l^{\mathrm{T}}\mathbf{p}_{k+l}\mathbf{z}_{k+l} \quad (l = 0, -1, \cdots, -m+1), \tag{B3}$$

$$\mathbf{t}_{l-1} = \mathbf{t}_l - \rho_{k+l}\mathbf{t}_l^{\mathrm{T}}\mathbf{p}_{k+l}\mathbf{y}_{k+l} \quad (l = 0, -1, \cdots, -m+1), \tag{B4}$$

$$\mathbf{s}'_{-m} = \gamma_k \mathbf{s}_{-m}, \tag{B5}$$

$$\mathbf{t}'_{-m} = \gamma_k \mathbf{t}_{-m}, \tag{B6}$$

$$\mathbf{s}'_l = \mathbf{s}'_{l-1} - \rho_{k+l}\left(\mathbf{t}_l^{\mathrm{T}}\mathbf{p}_{k+l} - \mathbf{s}'^{\mathrm{T}}_{l-1}\mathbf{y}_{k+l}\right)\mathbf{p}_{k+l} \quad (l = -m+1, -m+2, \cdots, 0), \tag{B7}$$

$$\mathbf{t}'_l = \mathbf{t}'_{l-1} - \rho_{k+l}\left(\mathbf{t}_l^{\mathrm{T}}\mathbf{p}_{k+l} - \mathbf{s}'^{\mathrm{T}}_{l-1}\mathbf{y}_{k+l}\right)\mathbf{q}_{k+l} \quad (l = -m+1, -m+2, \cdots, 0), \tag{B8}$$

$$\mathbf{d}_k = \mathbf{s}'_0, \tag{B9}$$

$$\mathbf{q}_k = \alpha_k \mathbf{t}'_0. \tag{B10}$$

Appendix C: Pseudo observation sites

Table C.1. List of pseudo observation sites used in the identical twin experiment

Site name	Latitude [deg.]	Longitude [deg.]	Altitude [m]
Alert	82.45	-62.51	205
Ny-Alesund	78.91	11.89	479
Mould Bay	76.25	-119.35	35
Summit	72.60	-38.42	3214
Barrow	71.32	-156.61	16
Pallas-Sammaltunturi	67.97	24.12	565
Ocean Station M	66.00	2.00	0
Storhofdi	63.40	-20.29	127
Churchill	58.75	-94.01	35
Baltic Sea	55.35	17.22	28
Cold Bay	55.21	-162.72	57
Mace Head	53.33	-9.90	26
Shemya Island	52.71	174.13	28
Ile Grande	48.80	-3.58	15
Hohenpeissenberg	47.80	11.02	941
Ulaan Uul	44.45	111.10	1012
Black Sea	44.18	28.66	5
Plateau Assy	43.25	77.88	2524
Cape Ochi-ishi	43.15	145.50	50
Begur	41.97	3.23	16
Centro de Investigacion de la Baja Atmosfera	41.81	-4.93	850
Niwot Ridge	40.05	-105.59	3526
Wendover	39.90	-113.72	1332
Point Arena	38.95	-123.74	22
Terceira Island	38.77	-27.38	24
Tae-ahn Peninsula	36.74	126.13	21
Mt. Waliguan	36.29	100.90	3815

Table C.1. (continued)

Site name	Latitude [deg.]	Longitude [deg.]	Altitude [m]
Lampedusa	35.52	12.62	50
Finokalia	35.34	25.67	155
La Jolla	32.90	-117.30	15
Tudor Hill	32.26	-64.88	35
WIS Station	30.86	34.78	482
Izana	28.31	-16.50	2377
Sand Island	28.21	-177.38	15
Key Biscayne	25.67	-80.16	6
Yonagunijima	24.47	123.02	50
Minamitorishima	24.28	153.98	28
Assekrem	23.26	5.63	2715
Mauna Loa	19.54	-155.58	3402
Cape Kumukahi	19.52	-154.82	8
High Altitude Global Climate Observation Center	18.98	-97.31	4469
Cape Rama	15.08	73.83	65
Mariana Islands	13.39	144.66	5
Ragged Point	13.16	-59.43	20
Christmas Island	1.70	-157.15	5
Mt. Kenya	-0.06	37.30	3649
Mahe Island	-4.68	55.53	6
Ascension Island	-7.97	-14.40	90
Arembepe	-12.77	-38.17	6
Tutuila	-14.25	-170.56	47
Cape Ferguson	-19.28	147.06	7
Easter Island	-27.16	-109.43	69
Cape Point	-34.35	18.49	260
Cape Grim	-40.68	144.69	164
Baring Head Station	-41.41	174.87	85
Crozet Island	-46.43	51.85	202
Macquarie Island	-54.48	158.97	11
Tierra Del Fuego	-54.85	-68.31	17
Drake Passage	-59.00	-64.69	5

Table C.1. (continued)

Site name	Latitude [deg.]	Longitude [deg.]	Altitude [m]
Palmer Station	-64.92	-64.00	15
Casey	-66.28	110.52	52
Mawson Station	-67.62	62.87	37
Syowa Station	-69.00	39.58	3
Halley Station	-75.61	-26.21	33
South Pole	-89.98	-24.80	2815

Acknowledgements. ~~We~~ Comments from Maarten Krol and an anonymous reviewer helped to improve the manuscript. They are greatly appreciated. We also thank Kaz Higuchi of York University, Canada, for his fruitful comments on the manuscript. This study is supported mainly by the Environment Research and Technology Development Fund (2-1401) of the Ministry of the Environment, Japan. This study is also supported partly by the cooperative research for climate system of Atmosphere and Ocean Research Institute, the University of Tokyo, by the research collaboration of the Institute of Statistical Mathematics, and by "advancement of meteorological and global environmental predictions utilizing observational ‘Big Data’” of the social and scientific priority issues (Theme 4) to be tackled by using ~~post~~ Post K computer of the FLAGSHIP2020 Project. The calculations of this study were performed on the super computer system, FUJITSU PRIMEHPC FX100, of Meteorological Research Institute.

References

Andres, R. J., Boden, T., and Marland, G.: Monthly Fossil-Fuel CO_2 Emissions: Mass of Emissions Gridded by One Degree Latitude by One Degree Longitude, Carbon Dioxide Information Analysis Center, Oak Ridge National Laboratory, U.S. Department of Energy, Oak Ridge, Tenn., U.S.A., doi:10.3334/CDIAC/ffe.MonthlyMass.2013, 2013.

Andrews, A. E., Kofler, J. D., Trudeau, M. E., Williams, J. C., Neff, D. H., Masarie, K. A., Chao, D. Y., Kitzis, D. R., Novelli, P. C., Zhao, C. L., Dlugokencky, E. J., Lang, P. M., Crotwell, M. J., Fischer, M. L., Parker, M. J., Lee, J. T., Baumann, D. D., Desai, A. R., Stanier, C. O., Wekker, S. F. J. D., Wolfe, D. E., Munger, J. W., and Tans, P. P.: CO_2, CO, and CH_4 measurements from tall towers in the NOAA Earth System Research Laboratory's Global Greenhouse Gas Reference Network: instrumentation, uncertainty analysis, and recommendations for future high-accuracy greenhouse gas monitoring efforts, Atoms. Meas. Tech., 7, 647–687, doi:10.5194/amt-7-647-2014, 2014.

Baker, D. F., Doney, S. C., and Schimel, D. S.: Variational data assimilation for atmospheric CO_2, Tellus, 58B, 359–365, doi:10.1111/j.1600-0889.2006.00218.x, 2006a.

Baker, D. F., Law, R. M., Gurney, K. R., Rayner, P., Peylin, P., Denning, A. S., Bousquet, P., Bruhwiler, L., Chen, Y., Ciais, P., Fung, I. Y., Heimann, M., John, J., Maki, T., Maksyutov, S., Masarie, K., Prather, M., Pak, B., Taguchi, S., and Zhu, Z.: TransCom 3 inversion intercomparison: Impact of transport model errors on the interannual variability of regional CO_2 fluxes, 1988–2003, Global Biogeochem. Cycles, 20, doi:10.1029/2004GB002439, 2006b.

Basu, S., Guerlet, S., Butz, A., Houweling, S., Hasekamp, O., Aben, I., Krummel, P., Steele, P., Langenfelds, R., Torn, M., Biraud, S., Stephens, B., Andrews, A., and Worthy, D.: Global CO_2 fluxes estimated from GOSAT retrievals of total column CO_2, Atoms. Chem. Phys., 13, 8695–8717, doi:10.5194/acp-13-8695-2013, 2013.

Bergamaschi, P., Houweling, S., Segers, A., Krol, M., Frankenberg, C., Scheepmaker, R. A., Dlugokencky, E., Wofsy, S. C., Kort, E. A., Sweeney, C., Schuck, T., Brenninkmeijer, C., Chen, H., Beck, V., and Gerbig, C.: Atmospheric CH_4 in the first decade of the 21st century: Inverse modeling analysis using SCIAMACHY satellite retrievals and NOAA surface measurements, J. Geophys. Res., 118, 7350–7369, doi:10.1002/jgrd.50480, 2013.

Chevallier, F., Fisher, M., Peylin, P., Serrar, S., Bousquet, P., Bréon, F.-M., Chédin, A., and Ciais, P.: Inferring CO_2 sources and sinks from satellite observations: Method and application to TOVS data, J. Geophys. Res., 110, doi:10.1029/2005JD006390, 2005.

Chevallier, F., Bréon, F.-M., and Rayner, P. J.: Contribution of the Orbiting Carbon Observatory to the estimation of CO_2 sources and sinks: Theoretical study in a variational data assimilation framework, J. Geophys. Res., 112, doi:10.1029/2006JD007375, 2007.

Chevallier, F., Wang, T., Ciais, P., Maignan, F., Bocquet, M., Altaf Arain, M., Cescatti, A., Chen, J., Dolman, A. J., Law, B. E., Margolis, H. A., Montagnani, L., and Moors, E. J.: What eddy-covariance measurements tell us about prior land flux errors in CO_2-flux inversion schemes, Global Biogeochem. Cycles, 26, doi:10.1029/2010GB003974, 2012.

Conway, T. J., Tans, P. P., Waterman, L. S., Thoning, K. W., Kitzis, D. R., Masarie, K. A., and Zhang, N.: Evidence for interannual variability of the carbon cycle from the National Oceanic and Atmospheric Administration/Climate Monitoring and Diagnostics Laboratory Global Air Sampling Network, J. Geophys. Res., 99, 22 831–22 855, doi:10.1029/94JD01951, 1994.

Dee, D. P., Uppala, S. M., Simmons, A. J., Berrisford, P., Poli, P., Kobayashi, S., Andrae, U., Balmaseda, M. A., Balsamo, G., Bauer, P., Bechtold, P., Beljaars, A. C. M., van de Berg, L., Bidlot, J., Bormann, N., Delsol, C., Dragani, R., Fuentes, M., Geer, A. J., Haimberger, L., Healy, S. B., Hersbach, H., Hólm, E. V., Isaksen, L., Kållberg, P., Köhler, M., Matricardi, M., McNally, A. P., Monge-Sanz, B. M., Morcrette, J.-J., Park, B.-K., Peubey, C., de Rosnay, P., Tavolato, C., Thépaut, J.-N., and Vitart, F.: The ERA-Interim reanalysis: configuration and performance of the data assimilation system, Quart. J. Roy. Meteor. Soc., 137, 553–597, doi:10.1002/qj.828, 2011.

Derber, J. and Rosati, A.: A Global Oceanic Data Assimilation System, J. Phys. Oceanogr., 19, 1333–1347, 1989.

Enting, I. G.: Inverse Problems in Atmospheric Constituent Transport, Cambridge University Press, New York, 2002.

Fujii, Y.: Preconditioned Optimizing Utility for Large-dimensional analyses (POpULar), J. Oceanogr., 61, 167–181, doi:10.1007/s10872-005-0029-z, 2005.

Fujii, Y. and Kamachi, M.: A nonlinear preconditioned quasi-Newton method without inversion of a first-guess covariance matrix in variational analyses, Tellus A, 55, 450–454, doi:10.1034/j.1600-0870.2003.00030.x, 2003.

Gou, T. and Sandu, A.: Continuous versus discrete advection adjoints in chemical data assimilation with CMAQ, Atmos. Environ., 45, 4868–4881, doi:10.1016/j.atmosenv.2011.06.015, 2011.

Gurney, K. R., Law, R. M., Denning, A. S., Rayner, P. J., Baker, D., Bousquet, P., Bruhwiler, L., Chen, Y.-H., Ciais, P., Fan, S., Fung, I. Y., Gloor, M., Heimann, M., Higuchi, K., John, J., Maki, T., Maksyutov, S., Masarie, K., Peylin, P., Prather, M., Pak, B. C., Randerson, J., Sarmiento, J., Taguchi, S., Takahashi, T., and Yuen, C.-W.: Towards robust regional estimates of CO_2 sources and sinks using atmospheric transport models, Nature, 415, 626–630, doi:10.1038/415626a, 2002.

Hooghiemstra, P. B., Krol, M. C., Bergamaschi, P., Laat, A. T. J., Werf, G. R., Novelli, P. C., Deeter, M. N., Aben, I., and Röckmann, T.: Comparing optimized CO emission estimates using MOPITT or NOAA surface network observations, J. Geophys. Res., 117, doi:10.1029/2011JD017043, 2012.

Iida, Y., Kojima, A., Takatani, Y., Nakano, T., Sugimoto, H., Midorikawa, T., and Ishii, M.: Trends in pCO_2 and sea–air CO_2 flux over the global open oceans for the last two decades, J. Oceanogr., 71, doi:10.1007/s10872-015-0306-4, 2015.

Ito, A. and Inatomi, M.: Use of a process-based model for assessing the methane budgets of global terrestrial ecosystems and evaluation of uncertainty, Biogeosciences, 9, 759–773, doi:10.5194/bg-9-759-2012, 2012.

Kato, E., Kinoshita, T., Ito, A., Kawamiya, M., and Yamagata, Y.: Evaluation of spatially explicit emission scenario of land-use change and biomass burning using a process-based biogeochemical model, Journal of Land Use Science, 8, 104–122, doi:10.1080/1747423X.2011.628705, 2013.

Kobayashi, S., Ota, Y., Harada, Y., Ebita, A., Moriya, M., Onoda, H., Onogi, K., Kamahori, H., Kobayashi, C., Endo, H., Miyaoka, K., and Takahashi, K.: The JRA-55 Reanalysis: General Specifications and Basic Characteristics, J. Meteor. Soc. Japan, 93, 5–48, doi:10.2151/jmsj.2015-001, 2015.

Kopacz, M., Jacob, D. J., Fisher, J. A., Logan, J. A., Zhang, L., Megretskaia, I. A., Yantosca, R. M., Singh, K., Henze, D. K., Burrows, J. P., Buchwitz, M., Khlystova, I., McMillan, W. W., Gille, J. C., Edwards, D. P., Eldering, A., Thouret, V., and Nedelec, P.: Global estimates of CO sources with high resolution by adjoint inversion of multiple satellite datasets (MOPITT, AIRS, SCIAMACHY, TES), Atoms. Chem. Phys., 10, 855–876, doi:10.5194/acp-10-855-2010, 2010.

Law, R. M., Peters, W., Rödenbeck, C., Aulagnier, C., Baker, I., Bergmann, D. J., Bousquet, P., Brandt, J., Bruhwiler, L., Cameron-Smith, P. J., Christensen, J. H., Delage, F., Denning, A. S., Fan, S., Geels, C., Houweling, S., Imasu, R., Karstens, U., Kawa, S. R., Kleist, J., Krol, M. C., Lin, S.-J., Lokupitiya, R., Maki, T., Maksyutov, S., Niwa, Y., Onishi, R., Parazoo, N., Patra, P. K., Pieterse, G., Rivier, L., Satoh, M., Serrar, S., Taguchi, S., Takigawa, M., Vautard, R., Vermeulen, A. T., and Zhu, Z.: TransCom model simulations of hourly atmospheric CO_2: Experimental overview and diurnal cycle results for 2002, Global Biogeochem. Cycles, 22, doi:10.1029/2007GB003050, 2008.

Lewis, S. L., Brando, P. M., Phillips, O. L., van der Heijden, G. M. F., and Nepstad, D.: The 2010 Amazon Drought, Science, 331, 554–554, doi:10.1126/science.1200807, 2011.

Liu, D. C. and Nocedal, J.: On the limited memory BFGS method for large scale optimization, Mathematical Programming, 45, 503–528, doi:10.1007/BF01589116, 1989.

Liu, J., Bowman, K., Lee, M., Henze, D., Bousserez, N., Brix, H., Collatz, G. J., Menemenlis, D., Ott, L., Pawson, S., Jones, D., and Nassar, R.: Carbon monitoring system flux estimation and attribution: impact of ACOS-GOSAT XCO_2 sampling on the inference of terrestrial biospheric sources and sinks, Tellus B, 66, doi:10.3402/tellusb.v66.22486, 2014.

Lorenc, A. C.: Optimal nonlinear objective analysis, Quart. J. Roy. Meteor. Soc., 114, 205–240, doi:10.1002/qj.49711447911, 1988.

Machida, T., Matsueda, H., Sawa, Y., Nakagawa, Y., Hirotani, K., Kondo, N., Goto, K., Nakazawa, T., Ishikawa, K., and Ogawa, T.: Worldwide Measurements of Atmospheric CO_2 and Other Trace Gas Species Using Commercial Airlines, J. Atmos. Oceanic Technol., 25, 1744–1754, doi:10.1175/2008JTECHA1082.1, 2008.

Matsueda, H., Machida, T., Sawa, Y., and Niwa, Y.: Long-term change of CO_2 latitudinal distribution in the upper troposphere, Geophys. Res. Lett., 42, 2508–2514, doi:10.1002/2014GL062768, 2015.

Meirink, J. F., Bergamaschi, P., Frankenberg, C., d'Amelio, M. T. S., Dlugokencky, E. J., Gatti, L. V., Houweling, S., Miller, J. B., Röckmann, T., Villani, M. G., and Krol, M. C.: Four-dimensional variational data assimilation for inverse modeling of atmospheric methane emissions: Analysis of SCIAMACHY observation, J. Geophys. Res., 113, doi:10.1029/2007JD009740, 2008.

Niwa, Y., Patra, P. K., Sawa, Y., Machida, T., Matsueda, H., Belikov, D., Maki, T., Ikegami, M., Imasu, R., Maksyutov, S., Oda, T., Satoh, M., and Takigawa, M.: Three-dimensional variations of atmospheric CO_2: aircraft measurements and multi-transport model simulations, Atoms. Chem. Phys., 11, 13 359–13 375, doi:10.5194/acp-11-13359-2011, 2011a.

Niwa, Y., Tomita, H., Satoh, M., and Imasu, R.: A Three-Dimensional Icosahedral Grid Advection Scheme Preserving Monotonicity and Consistency with Continuity for Atmospheric Tracer Transport, J. Meteor. Soc. Japan, 89, 255–268, doi:10.2151/jmsj.2011-306, 2011b.

Niwa, Y., Machida, T., Sawa, Y., Matsueda, H., Schuck, T. J., Brenninkmeijer, C. A. M., Imasu, R., and Satoh, M.: Imposing strong constraints on tropical terrestrial CO_2 fluxes using passenger aircraft based measurements, J. Geophys. Res., 117, doi:10.1029/2012JD017474, 2012.

Niwa, Y., Hirofumi, T., Satoh, M., Imasu, R., Sawa, Y., Tsuboi, K., Matsueda, H., Machida, T., Sasakawa, M., Belan, B., and Saigusa, N.: A 4D-Var inversion system based on an icosahedral grid model (NICAM-TM 4D-Var v1.0): 1. Off-line forward and adjoint transport models, manuscript submitted for publication, 2016.

Niwa, Y., Tomita, H., Satoh, M., Imasu, R., Sawa, Y., Tsuboi, K., Matsueda, H., Machida, T., Sasakawa, M., Belan, B., and Saigusa, N.: A 4D-Var inversion system based on the icosahedral grid model (NICAM-TM 4D-Var v1.0) – Part 1: Offline forward and adjoint transport models, Geosci. Model Dev., 10, 1157–1174, doi:10.5194/gmd-10-1157-2017, 2017.

Nocedal, J.: Updating quasi-Newton matrices with limited storage, Mathematics of Computation, 35, 773–782, doi:10.1090/S0025-5718-1980-0572855-7, 1980.

Nocedal, J. and Wright, S. J.: Numerical Optimization (2nd edn), Springer, New York, 2006.

Onogi, K., Tsutsui, J., Koide, H., Sakamoto, M., Kobayashi, S., Hatsushika, H., Matsumoto, T., Yamazaki, N., Kamahori, H., Takahashi, K., Kadokura, S., Wada, K., Kato, K., Oyama, R., Ose, T., Mannoji, N., and Taira, R.: The JRA-25 Reanalysis, J. Meteor. Soc. Japan, 85, 369–432, doi:10.2151/jmsj.85.369, 2007.

Patra, P. K., Law, R. M., Peters, W., Rödenbeck, C., Takigawa, M., Aulagnier, C., Baker, I., Bergmann, D. J., Bousquet, P., Brandt, J., Bruhwiler, L., Cameron-Smith, P. J., Christensen, J. H., Delage, F., Denning, A. S., Fan, S., Geels, C., Houweling, S., Imasu, R., Karstens, U., Kawa, S. R., Kleist, J., Krol, M. C., Lin, S.-J., Lokupitiya, R., Maki, T., Maksyutov, S., Niwa, Y., Onishi, R., Parazoo, N., Pieterse, G., Rivier, L., Satoh, M., Serrar, S., Taguchi, S., Vautard, R., Vermeulen, A. T., and Zhu, Z.: TransCom model simulations of hourly atmospheric CO_2: Analysis of synoptic-scale variations of the period 2002-2003, Global Biogeochem. Cycles, 22, doi:10.1029/2007GB003081, 2008.

Peylin, P., Law, R. M., Gurney, K. R., Chevallier, F., Jacobson, A. R., Maki, T., Niwa, Y., Patra, P. K., Peters, W., Rayner, P. J., Rödenbeck, C., van der Laan-Luijkx, I. T., and Zhang, X.: Global atmospheric carbon budget: results from an ensemble of atmospheric CO_2 inversions, Biogeosciences, 10, 6699–6720, doi:10.5194/bg-10-6699-2013, 2013.

Randerson, J. T., Thompson, M. V., Conway, T. J., Fung, I. Y., and Field, C. B.: The contribution of terrestrial sources and sinks to trends in the seasonal cycle of atmospheric carbon dioxide, Global Biogeochem. Cycles, 11, 535–560, doi:10.1029/97GB02268, 1997.

Rayner, P. J., Enting, I. G., Francey, R. J., and Langenfelds, R.: Reconstructing the recent carbon cycle from atmospheric CO_2, δ13C and O_2/N_2 observations, Tellus B, 51, 213–232, doi:10.1034/j.1600-0889.1999.t01-1-00008.x, 1999.

Rödenbeck, C.: Estimating CO_2 sources and sinks from atmospheric mixing ratio measurements using a global inversion of atmospheric transport, Max-Planck-Institut für Biogeochemie: Technical Paper 6, 2005.

Saitoh, N., Kimoto, S., Sugimura, R., Imasu, R., Kawakami, S., Shiomi, K., Kuze, A., Machida, T., Sawa, Y., and Matsueda, H.: Algorithm update of the GOSAT/TANSO-FTS thermal infrared CO_2 product (version 1) and validation of the UTLS CO_2 data using CONTRAIL measurements, Atmospheric Measurement Techniques, 9, 2119–2134, doi:10.5194/amt-9-2119-2016, 2016.

Sasakawa, M., Shimoyama, K., Machida, T., Tsuda, N., Suto, H., Arshinov, M., Davydov, D., Fofonov, A., Krasnov, O., Saeki, T., Koyama, Y., and Maksyutov, S.: Continuous measurements of methane from a tower network over Siberia, Tellus B, 62, 403–416, doi:10.1111/j.1600-0889.2010.00494.x, 2010.

Satoh, M., Matsuno, T., Tomita, H., Miura, H., Nasuno, T., and Iga, S.: Nonhydrostatic icosahedral atmospheric model (NICAM) for global cloud resolving simulations, J. Comput. Phys., 227, 3486–3514, doi:10.1016/j.jcp.2007.02.006, 2008.

Satoh, M., Tomita, H., Yashiro, H., Miura, H., Kodama, C., Seiki, T., Noda, A. T., Yamada, Y., Goto, D., Sawada, M., Miyoshi, T., Niwa, Y., Hara, M., Ohno, T., Iga, S., Arakawa, T., Inoue, T., and Kubokawa, H.: The Non-hydrostatic Icosahedral Atmospheric Model: description and development, Progress in Earth and Planetary Science, 1, 1–32, doi:10.1186/s40645-014-0018-1, 2014.

Sawa, Y., Machida, T., Matsueda, H., Niwa, Y., Tsuboi, K., Murayama, S., Morimoto, S., and Aoki, S.: Seasonal changes of CO_2, CH_4, N_2O, and SF_6 in the upper troposphere/lower stratosphere over the Eurasian continent observed by commercial airliner, Geophys. Res. Lett., 42, 2001–2008, doi:10.1002/2014GL062734, 2015.

Shanno, D. F. and Phua, K.-H.: Matrix conditioning and nonlinear optimization, Math. Program., 14, 149–160, doi:10.1007/BF01588962, 1978.

Smedstad, O. M. and O'Brien, J. J.: Variational data assimilation and parameter estimation in an equatorial Pacific ocean model, Prog. Oceanog., 26, 179–241, doi:10.1016/0079-6611(91)90002-4, 1991.

Stammer, D., Wunsch, C., Giering, R., Eckert, C., Heimbach, P., Marotzke, J., Adcroft, A., Hill, C. N., and Marshall, J.: Global ocean circulation during 1992–1997, estimated from ocean observations and a general circulation model, J. Geophys. Res., 107, 1–1–1–27, doi:10.1029/2001JC000888, 3118, 2002.

Takahashi, T., Sutherland, S. C., Wanninkhof, R., Sweeney, C., Feely, R. A., Chipman, D. W., Hales, B., Friederich, G., Chavez, F., Sabine, C., Watson, A., Bakker, D. C., Schuster, U., Metzl, N., Yoshikawa-Inoue, H., Ishii, M., Midorikawa, T., Nojiri, Y., Körtzinger, A., Steinhoff, T., Hoppema, M., Olafsson, J., Arnarson, T. S., Tilbrook, B., Johannessen, T., Olsen, A., Bellerby, R., Wong, C., Delille, B., Bates, N., and de Baar, H. J.: Climatological mean and decadal change in surface ocean pCO_2, and net sea-air CO_2 flux over the global oceans, Deep-Sea Research, Part II, 56, 554–577, 2009.

Tarantola, A.: Inverse Problem Theory and Methods for Model Parameter Estimation, Society for Industrial and Applied Mathematics, Philadelphia, 2005.

Thuburn, J.: Multidimensional Flux-Limited Advection Schemes, J. Comput. Phys., 123, 74–83, doi:10.1006/jcph.1996.0006, 1996.

Tomita, H. and Satoh, M.: A new dynamical framework of nonhydrostatic global model using the icosahedral grid, Fluid Dyn. Res., 34, 357–400, doi:10.1016/j.fluiddyn.2004.03.003, 2004.

Usui, N., Ishizaki, S., Fujii, Y., Tsujino, H., Yasuda, T., and Kamachi, M.: Meteorological Research Institute multivariate ocean variational estimation (MOVE) system: Some early results, Advances in Space Research, 37, 806–822, doi:10.1016/j.asr.2005.09.022, 2006.

Usui, N., Fujii, Y., Sakamoto, K., and Kamachi, M.: Development of a Four-Dimensional Variational Assimilation System for Coastal Data Assimilation around Japan, Mon. Wea. Rev., 143, 3874–3892, doi:10.1175/MWR-D-14-00326.1, 2015.

van der Werf, G. R., Randerson, J. T., Giglio, L., Collatz, G. J., Mu, M., Kasibhatla, P. S., Morton, D. C., DeFries, R. S., Jin, Y., and van Leeuwen, T. T.: Global fire emissions and the contribution of deforestation, savanna, forest, agricultural, and peat fires (1997–2009), Atoms. Chem. Phys., 10, 11 707–11 735, doi:10.5194/acp-10-11707-2010, 2010.

Yoshida, Y., Kikuchi, N., Morino, I., Uchino, O., Oshchepkov, S., Bril, A., Saeki, T., Schutgens, N., Toon, G. C., Wunch, D., Roehl, C. M., Wennberg, P. O., Griffith, D. W. T., Deutscher, N. M., Warneke, T., Notholt, J., Robinson, J., Sherlock, V., Connor, B., Rettinger, M., Sussmann, R., Ahonen, P., Heikkinen, P., Kyrö, E., Mendonca, J., Strong, K., Hase, F., Dohe, S., and Yokota, T.: Improvement of the retrieval algorithm for GOSAT SWIR XCO_2 and XCH_4 and their validation using TCCON data, Atoms. Meas. Tech., 6, 1533–1547, doi:10.5194/amt-6-1533-2013, 2013.

Yumimoto, K. and Takemura, T.: The SPRINTARS version 3.80/4D-Var data assimilation system: development and inversion experiments based on the observing system simulation experiment framework, Geosci. Model Dev., 6, 2005–2022, doi:10.5194/gmd-6-2005-2013, 2013.

Table 1. Prior and true flux datasets (other than the fossil fuel emission) used in the identical twin experiment

	Description	Reference
True	*Land:*	
	NEP fluxes from CASA modified by inversion	Randerson et al. (1997), Niwa et al. (2012)
	Biomass burning emissions from GFED v3.1	van der Werf et al. (2010)
	Ocean:	
	Climatological ΔpCO_2 measurement-based fluxes	Takahashi et al. (2009)
Priror	*Land:*	
	NBP fluxes from VISIT	Ito and Inatomi (2012)
	Ocean:	
	ΔpCO_2 measurement-based fluxes	Iida et al. (2015)

Table 2. List of the eight sensitivity tests and the global root mean square errors (GRMSE) of each posterior flux for the global land, the global ocean, and the global total. The numbers in parenthesis are those of the prior flux.

No.	Model	Optimization scheme	Prior error covariance	GRMSE [10^{-7} mol m^{-2} s^{-1}]		
				Land (5.58)	Ocean (0.24)	Global (5.59)
(1)	LINEAR	DR89	diag.	4.09	0.25	4.10
(2)	~~NON-LINEAR~~ NONLINEAR	DR89	diag.	6.69	0.36	6.70
(3)	LINEAR	POpULar	diag.	4.09	0.25	4.10
(4)	~~NON-LINEAR~~ NONLINEAR	POpULar	diag.	4.06	0.24	4.07
(5)	LINEAR	DR89	off-diag.	3.29	0.20	3.30
(6)	~~NON-LINEAR~~ NONLINEAR	DR89	off-diag.	3.37	0.20	3.37
(7)	LINEAR	POpULar	off-diag.	3.29	0.20	3.30
(8)	~~NON-LINEAR~~ NONLINEAR	POpULar	off-diag.	3.20	0.20	3.21

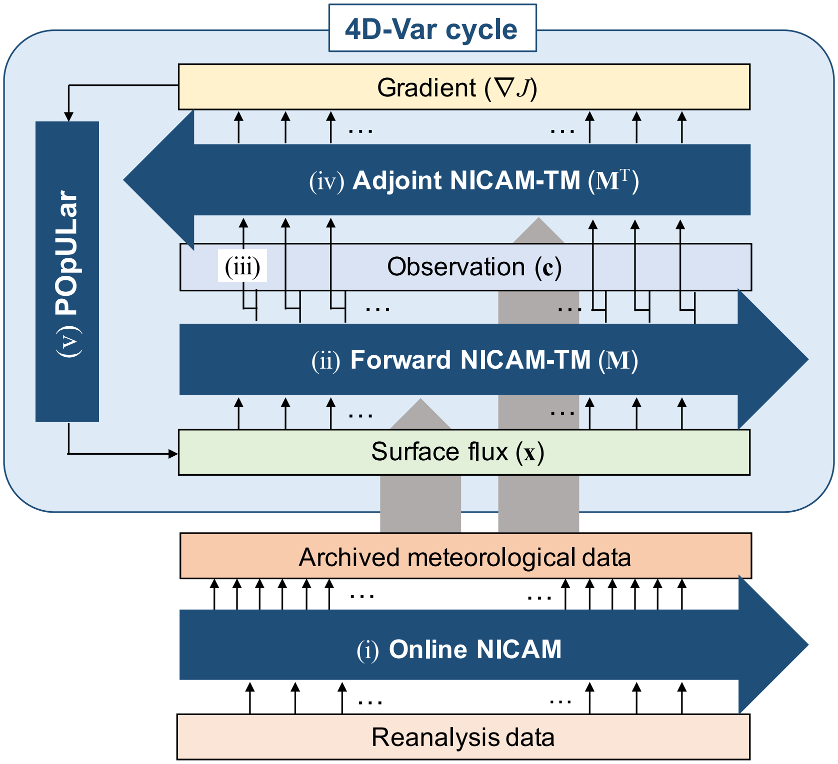

Figure 1. A schematic figure of NICAM-TM 4D-Var. A roman numeral indicates each calculation described in the text.

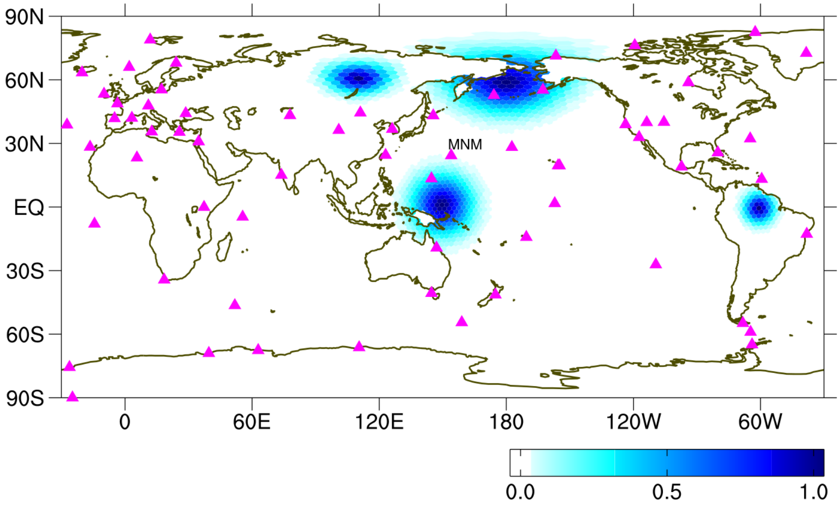

Figure 2. Locations of surface flask observation site (magenta triangle) and four distributions of error correlation introduced in the off-diagonal elements of **B**, which are centered at two land grids (60°N, 110°E and 60°N, 180°), and two ocean grids (0°, 150°E and 0°, 60°W), selected for example.

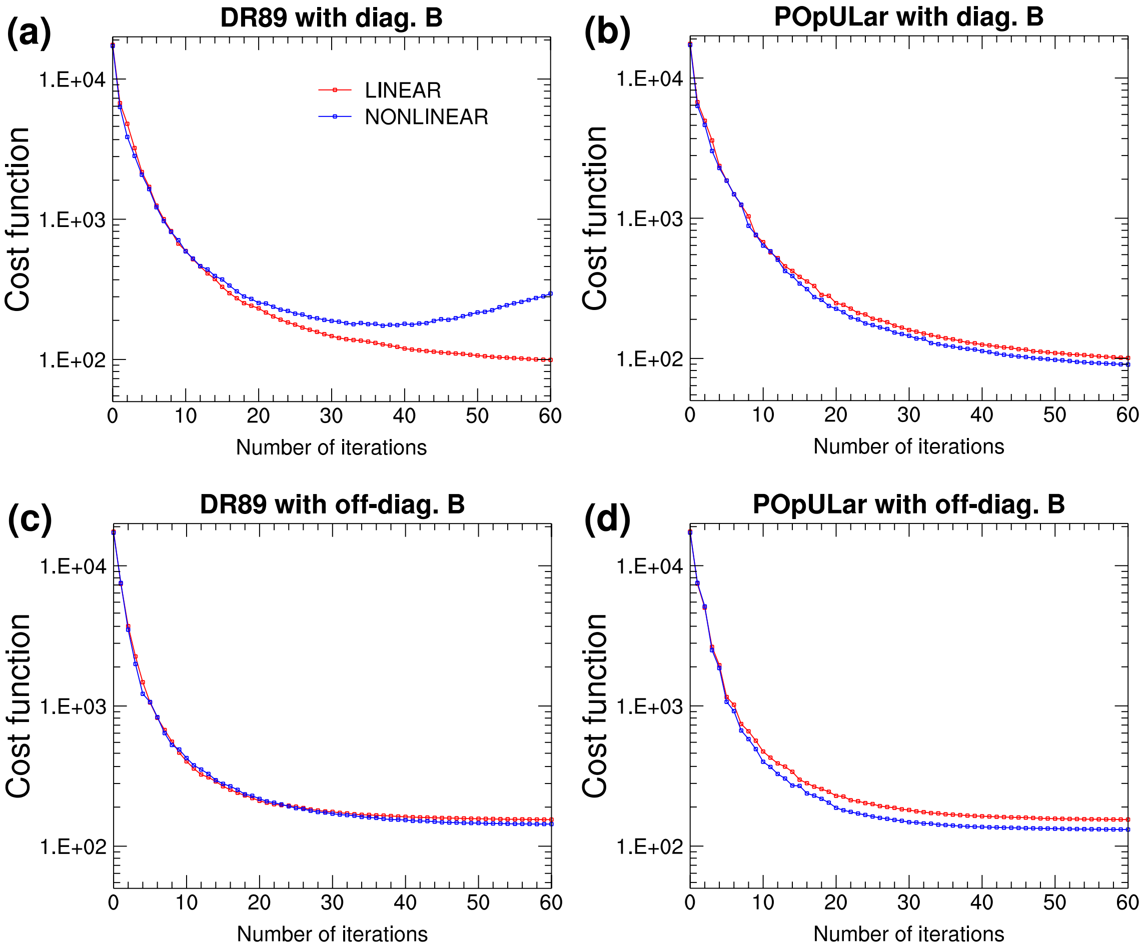

Figure 3. ~~Global root-mean-square error (GRMSE)~~ Cost function changes with iterations for the linear (red) and ~~non-linear~~ nonlinear (blue) models. Sensitivities to the optimization schemes (DR89: left, POpULar: right) and to the prior error covariance matrixes (diagonal: upper, off-diagonal: bottom) are shown.

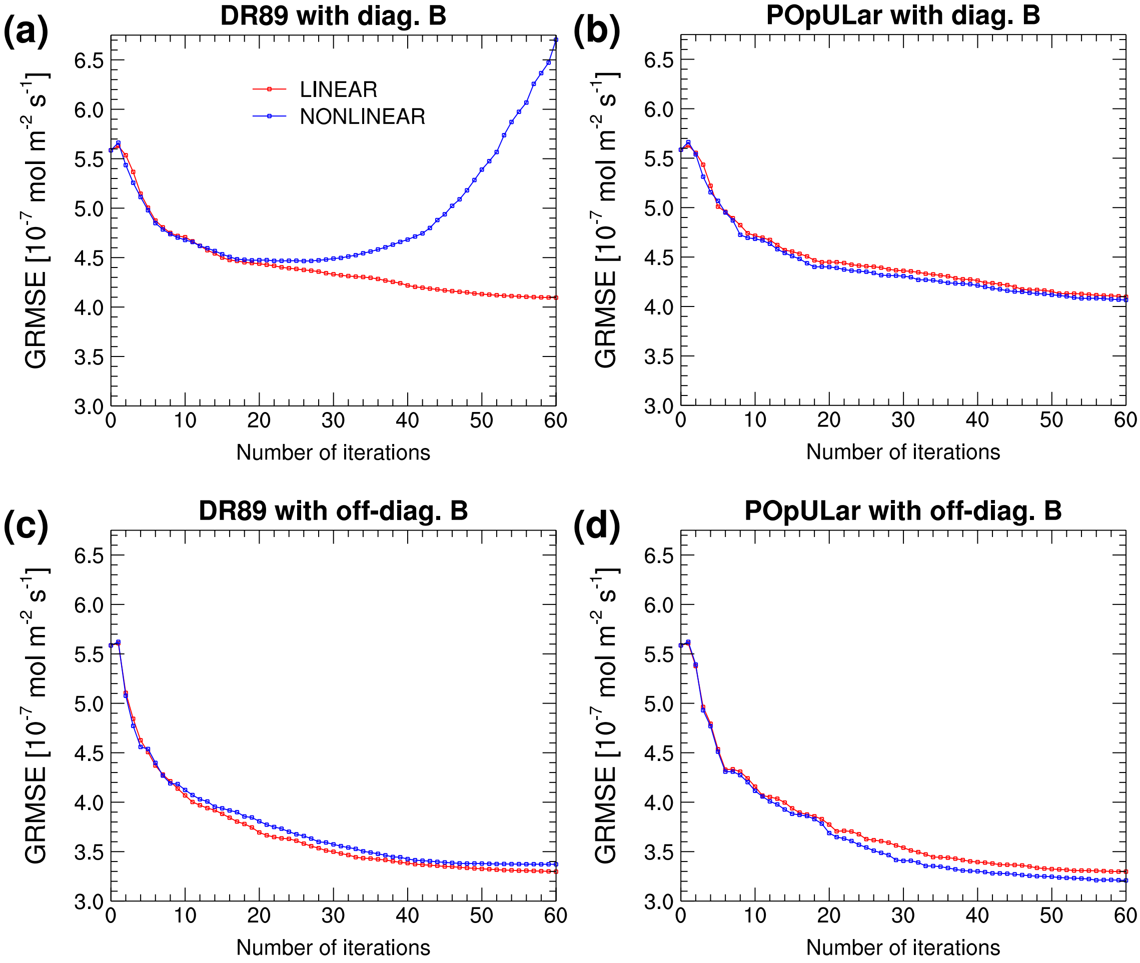

Figure 4. Same as Fig. 3, but for global root-mean-square error (GRMSE) changes with iterations.

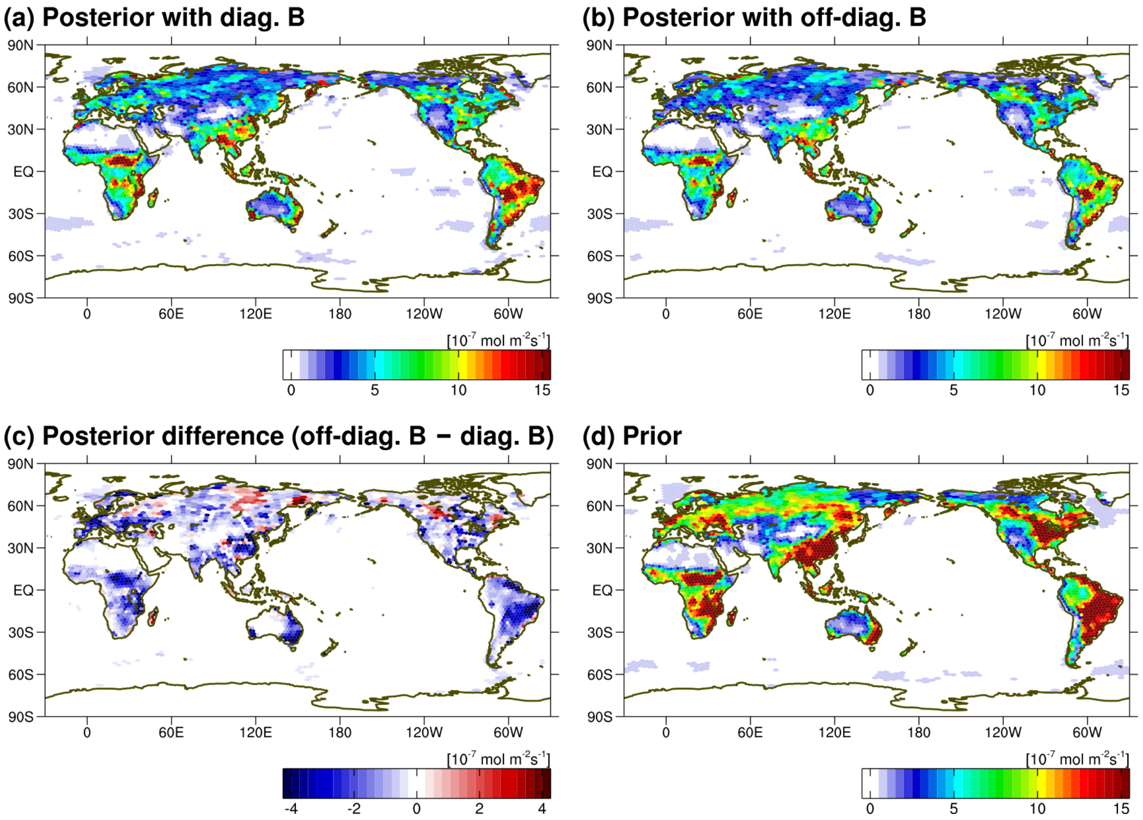

Figure 5. Root-mean-square error (RMSE) distributions of the posterior fluxes derived by POpULar+~~NON-LINEAR~~ NONLINEAR with the diagonal **B** (a) and the off-diagonal **B** (b). The difference between (b) and (a) is shown in (c) as well as the RMSE distribution of the prior flux (d).

~~Atmospheric CO_2 concentrations simulated by the forward NICAM-TM driven by the true, prior and posterior fluxes. The left panel shows the time series of concentrations at one observation site (Minamitorishima), located in the western North Pacific. Black open circles denote observations that are assimilated in the experiment, and green and blue lines represent CO_2 concentrations calculated from the prior and posterior fluxes, respectively. The right panel shows latitude-time cross sections of surface zonal averages calculated from the true (b), prior (c), and posterior fluxes (d).~~

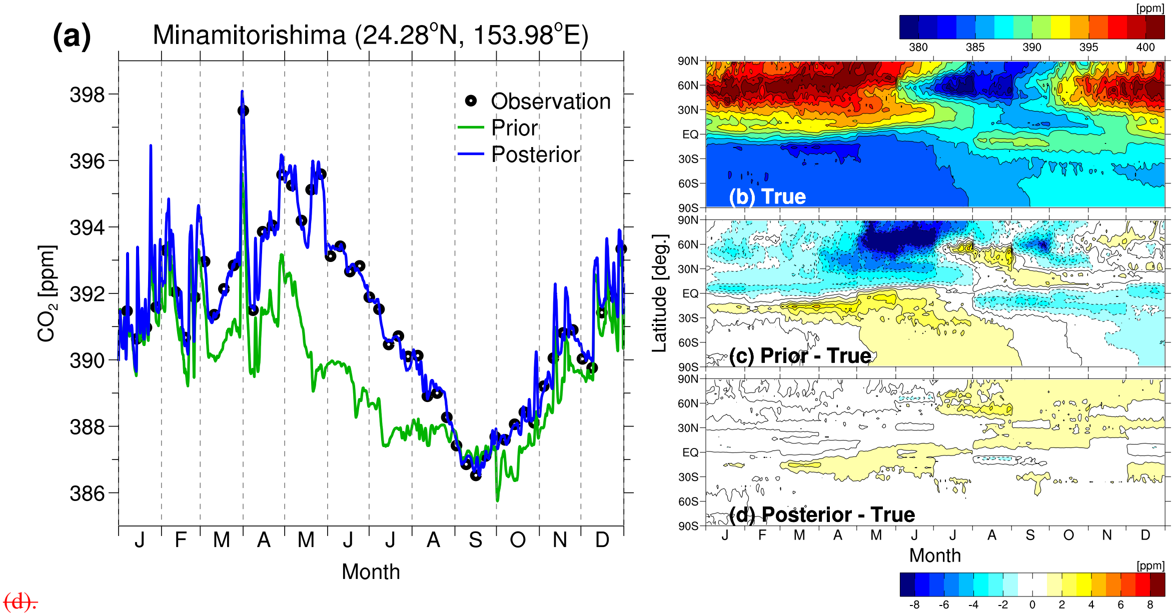

Figure 6. Atmospheric CO_2 concentrations simulated by the forward NICAM-TM driven by the true, prior and posterior fluxes. The left panel shows the time series of concentrations at the Minamitoshima observational site, located in the western North Pacific. Black open circles denote pseudo observations that are assimilated in the experiment, and green and blue lines represent CO_2 concentrations calculated from the prior and posterior fluxes, respectively. The right panel shows latitude-time cross sections of surface zonal averages calculated from the true flux (b), its differences from the concentration field generated by the prior flux (c) and by the posterior flux (d).

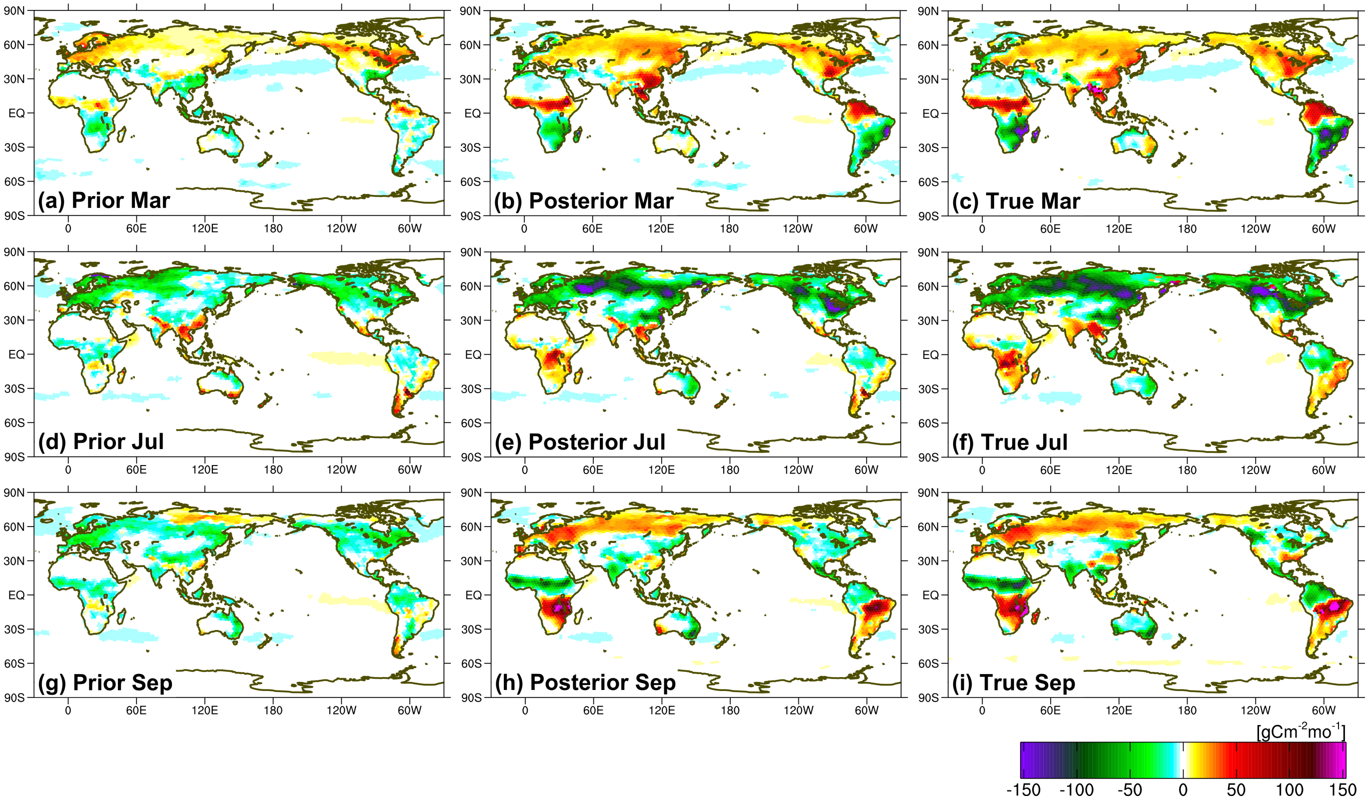

Figure 7. Monthly mean distributions of the prior (left), posterior (middle) and true (right) CO_2 fluxes. Fluxes are shown for March (a-c), July (d-f) and September (g-i) of 2010. Note that the fluxes do not include fossil fuel emissions, which are not optimized in the inversion.

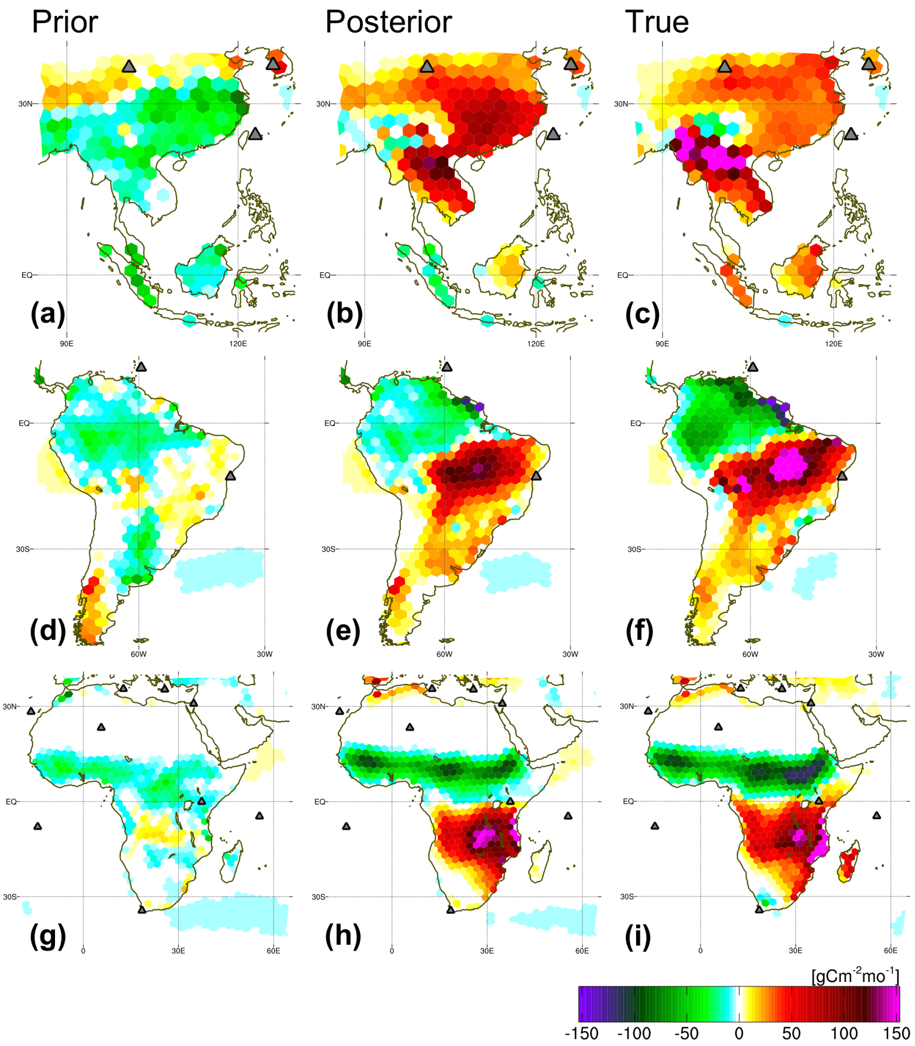

Figure 8. Same as Fig. ~~6~~7, but focused on regional flux anomalies due to biomass burnings for Southeast Asia in March (a-c), South America in September (d-f), and Africa in September (g-i). Gray triangles denote locations of the observational sites.

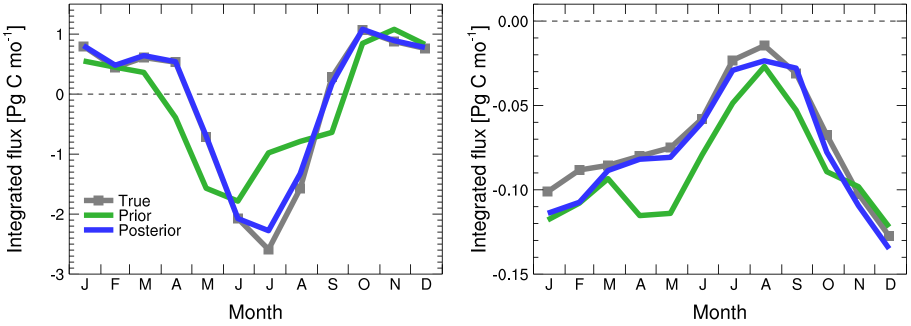

(a) Land 30−90°N

(b) Ocean 30−90°N

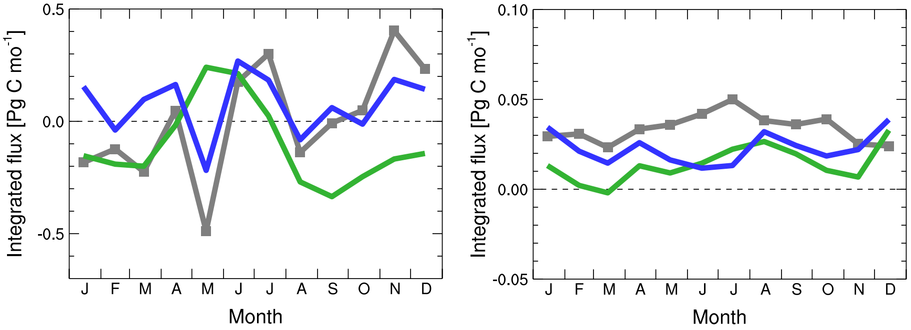

(c) Land 30°S−30°N

(d) Ocean 30°S−30°N

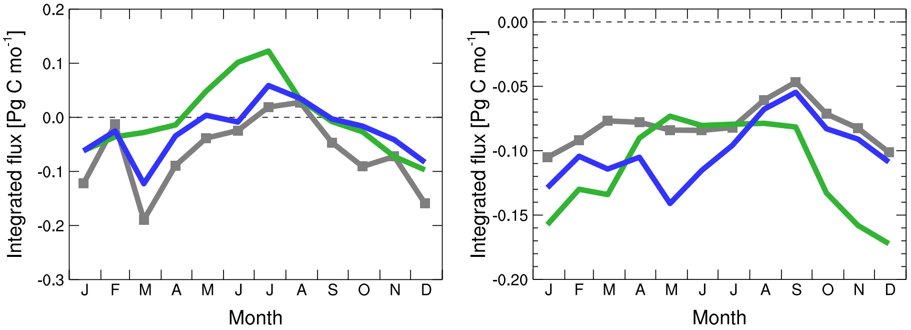

(e) Land 30−90°S

(f) Ocean 30−90°S

Figure 9. Monthly variations of the true (gray), prior (green) and posterior (blue) CO_2 fluxes integrated for latitude bands of 30–90°N (a,b), 30°S–30°N (c,d) and 30-90°S (e,f). Terrestrial (non-fossil fuel flux) (right) and ocean (left) fluxes are separately shown.

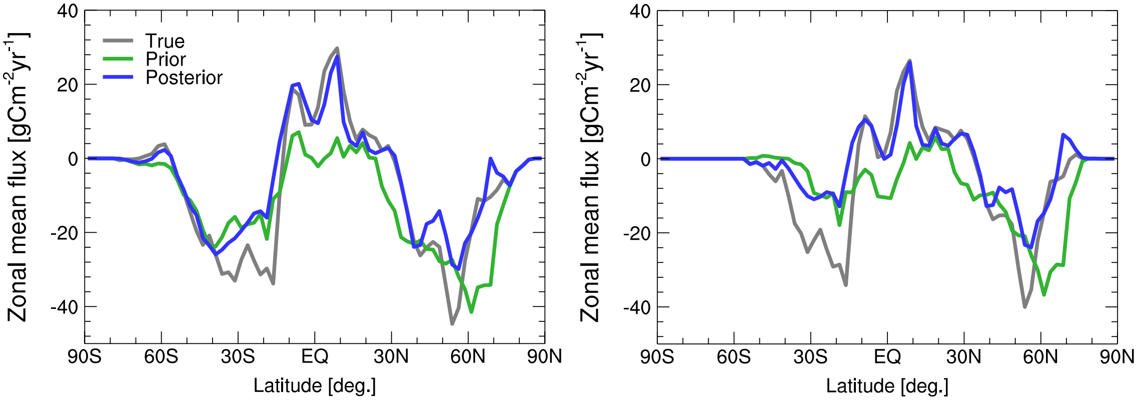
(a) Total

(b) Land

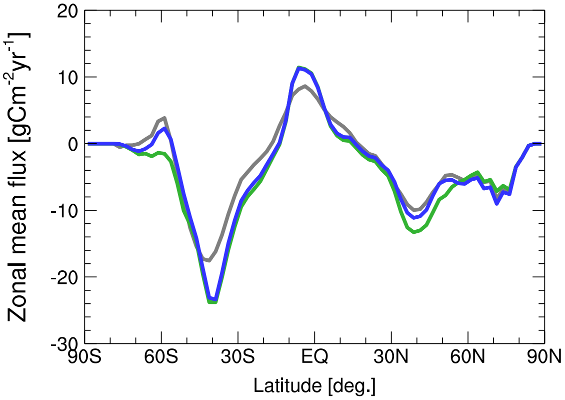
(c) Ocean

Figure 10. Latitudinal profiles of annual zonal mean CO_2 fluxes (gray: true, green: prior, blue: posterior), for the total (a), terrestrial (b) and ocean (c) areas. Note that fossil fuel emission is not included.